The Remote Effect of Typhoon Megi (2010) on the Heavy Rainfall over Northeastern Taiwan

TING-CHEN CHEN AND CHUN-CHIEH WU

Department of Atmospheric Sciences, National Taiwan University, Taipei, Taiwan

(Manuscript received 6 August 2015, in final form 3 June 2016)

ABSTRACT

The goal of this work is to improve understanding of the mechanisms leading to a heavy rainfall event under the combined influences of the outer circulation of Typhoon Megi (2010), the Asian monsoon, and the topography of Taiwan. Megi is a case featuring high forecast uncertainty associated with its sudden recurvature, along with remote heavy rainfall over northeastern Taiwan (especially at Yilan) and its adjacent seas during 19–23 October 2010. An ensemble simulation is conducted, and characteristic ensemble members are separated into subgroups based on either track accuracy or rainfall forecast skill. Comparisons between different subgroups are made to investigate favorable processes for precipitation and how the differences between these subgroups affect the rainfall simulation.

Several mechanisms leading to this remote rainfall event are shown. The northward transport of water vapor by Megi's outer circulation provides a moisture-laden environment over the coastal area of eastern Taiwan. Meanwhile, the outer circulation of Megi (with high θ_e) encounters the northeasterly monsoon (with low θ_e), and strong vertical motion is triggered through isentropic lifting in association with low-level frontogenesis over the ocean northeast of Yilan. Most importantly, the northeasterly flow advects the moisture inland to the steep mountains in south-southwestern Yilan, where strong orographic lifting further induces torrential rainfall. In addition, the analyses further attribute the uncertainty in simulating Megi's remote rainfall to several factors, including variations of storm track, strength and extension of the northeasterly monsoon, and, above all, the impinging angle of the upstream flow on the topography.

1. Introduction

One of the major hazards associated with tropical cyclones (TC) is the accompanying heavy rainfall, which often leads to devastating mudslides and floods, resulting in enormous economic loss and potential threats to human life. The quantitative precipitation forecast (QPF) associated with TCs remains a major challenge for numerical models, since the precipitation amount is affected by multiple factors, such as large-scale moisture distribution (e.g., Huang and Lin 2014); cloud microphysics (e.g., Yang et al. 2011); the internal structure of the TC (e.g., Wu et al. 2009; Lonfat et al. 2004); track variation (e.g., Lin et al. 2001; Zhang et al. 2010; Huang et al. 2011; Chien and Kuo 2011; Yen et al. 2011; Wang et al. 2012); TC–midlatitude interactions, such as extratropical transition (e.g., Atallah and Bosart 2003; Colle 2003; Jones et al. 2003); and the complicated interaction between the TC circulation and topography (e.g., Wu and Kuo 1999; Yu and Cheng 2008, 2013, 2014; C.-C. Wu et al. 2013; Huang and Lin 2014). In particular, the accuracy of TC track forecasts is often identified as a deciding factor in affecting the general forecast of typhoon-related rainfall, since the orography can modulate mesoscale rainfall distributions greatly, especially for landfalling cases (e.g., Chang et al. 1993; Wu and Kuo 1999; Marchok et al. 2007; Yu and Cheng 2008; Wang et al. 2009; Fang and Kuo 2013; C.-C. Wu et al. 2013).

In general, TC-related rainfall can be categorized into two types: direct and indirect. The former indicates that the precipitation is mainly caused by the TC circulation itself, while the latter is related to rainfall events associated with strong interactions between the TC and other synoptic or large-scale systems, such as an upper-level trough or monsoon system. As the indirect rainfall event may occur at a distance of hundreds of kilometers from the TC center, it is also referred to as the remote effect

Corresponding author address: Chun-Chieh Wu, Department of Atmospheric Sciences, National Taiwan University, No. 1, Sec. 4, Roosevelt Rd., Taipei 10617, Taiwan.
E-mail: cwu@typhoon.as.ntu.edu.tw

DOI: 10.1175/MWR-D-15-0269.1

of a TC on precipitation (e.g., Wang et al. 2009). In the western North Pacific (WNP), TCs are usually accompanied by a large-scale Asian monsoon circulation, and thus remote/indirect rainfall events are often favored in Taiwan because of the TC–monsoon interaction (e.g., Lin et al. 2001; Chien et al. 2008; Lee et al. 2008; Wu et al. 2009; Huang and Lin 2014; Yu and Cheng 2014).

The southwesterly monsoonal flow, which prevails during summer, can be enhanced by the outer circulation of a TC when it passes through Taiwan or approaches the boundary between the WNP and the South China Sea. Lin et al. (2001) documented a case study for a heavy rainfall event associated with Tropical Storm Rachel (1999) based on reanalysis data. They showed that, when the TC was located about 500 km to the southwest of Taiwan, the approaching storm strengthened the low-level southwesterly monsoonal flow. With strong inflow, orographic lifting over land induced vigorous convection that was not directly embedded in the approaching TC. Yu and Cheng (2014) investigated six typhoon cases and identified the characteristic features for typhoon-enhanced southwesterly flow and their impacts on intense rainfall under the interaction between the TC circulation and the summer monsoon. They showed that the orographic enhancement of precipitation in typhoon cases that have stronger interaction with the southwesterly monsoon, accompanied by stronger low-level upstream flow, appears to be more pronounced than in cases with weaker or no TC–monsoon interaction.

During autumn or early winter, the southwesterly monsoon that prevails in summer is replaced by northeasterly flow over East Asia. If a TC is located near the Philippines or the South China Sea, the warm, moist air advected northward by the outer circulation of TC can converge with the cold, dry winter northeasterly monsoon, resulting in a frontal-type convective system that causes intense rainfall in the eastern and/or northeastern region of Taiwan (Wu et al. 2009). Wu et al. (2009) used a schematic diagram to illustrate two major modes of rainfall events associated with Typhoon Babs (1998): one is described as the monsoon mode, resulting from the low-level convergence between the typhoon circulation and the monsoonal northeasterlies, and the other is designated as the topographic mode, which refers to the impingement of the typhoon circulation on the mountains as the major precipitation mechanism. In the United States, a TC remote rainfall event is referred to as a predecessor rain event (PRE; e.g., Cote 2007; Galarneau et al. 2010; Schumacher and Galarneau 2012), in which a long-lived, quasi-stationary mesoscale convective system is produced in connection with frontogenetical forcing, resulting in heavy rainfall before the approach of the storm itself.

To address the predictability and forecast uncertainty, ensemble simulations have recently been applied to TC-related rainfall issues (e.g., Zhang et al. 2010; Fang et al. 2011; Fang and Kuo 2013; C.-C. Wu et al. 2013). C.-C. Wu et al. (2013) investigated the impact of differences in TC track on rainfall amounts and distribution in an ensemble simulation during Typhoon Sinlaku (2009), suggesting that the uncertainties in rainfall patterns and amounts is highly related to the ensemble track variation. Note that most TC-related precipitation studies are associated with landfalling cases (i.e., a TC's direct effect on precipitation). Studies of a TC's remote rainfall effect and the associated forecast uncertainty are relatively limited. Previous studies (e.g., Wu et al. 2009; Galarneau et al. 2010) also showed that recurving TCs are more likely to cause a remote/indirect rainfall event to the far north of the main TC circulation, as compared to nonrecurving TCs. Using global ensemble forecasts, Schumacher and Galarneau (2012) analyzed the difference of TCs' impacts on moisture transport into the environment of PREs over the central United States between recurving and nonrecurving TCs. Ensemble members with TC recurvature feature larger amounts of moisture over the PRE region (above 20 mm higher) as compared to those without TC recurvature, but they do not necessarily feature larger amounts of rainfall associated with PREs. Based on these results, they suggested that, in addition to TC track and the corresponding moisture transport, the timing, location, and magnitude of ascent associated with synoptic- and mesoscale processes (e.g., frontogenetical forcing) are important in determining rainfall forecast.

To further study TC remote rainfall, a case study based on an ensemble simulation is conducted on Typhoon Megi (2010), a case featuring a sudden track recurvature in the South China Sea and remote heavy rainfall over the northeastern part of Taiwan during the northeasterly monsoon season (Figs. 1a,b). Since Megi tracked to the west of Taiwan, the torrential rainfall is hypothesized to have been caused by the interaction between Megi's outer circulation, the northeasterly monsoon, and the terrain of Taiwan. The main objective of this work is to evaluate the mechanisms leading to this remote torrential rainfall and to examine which key factors affect the QPF uncertainty in this case.

The remainder of this paper proceeds as follows. A brief overview of Megi is provided in section 2. The model configuration and experimental design are described in section 3. Section 4 presents the simulation results, including the identified favorable processes as well as the forecast uncertainty of this remote rainfall

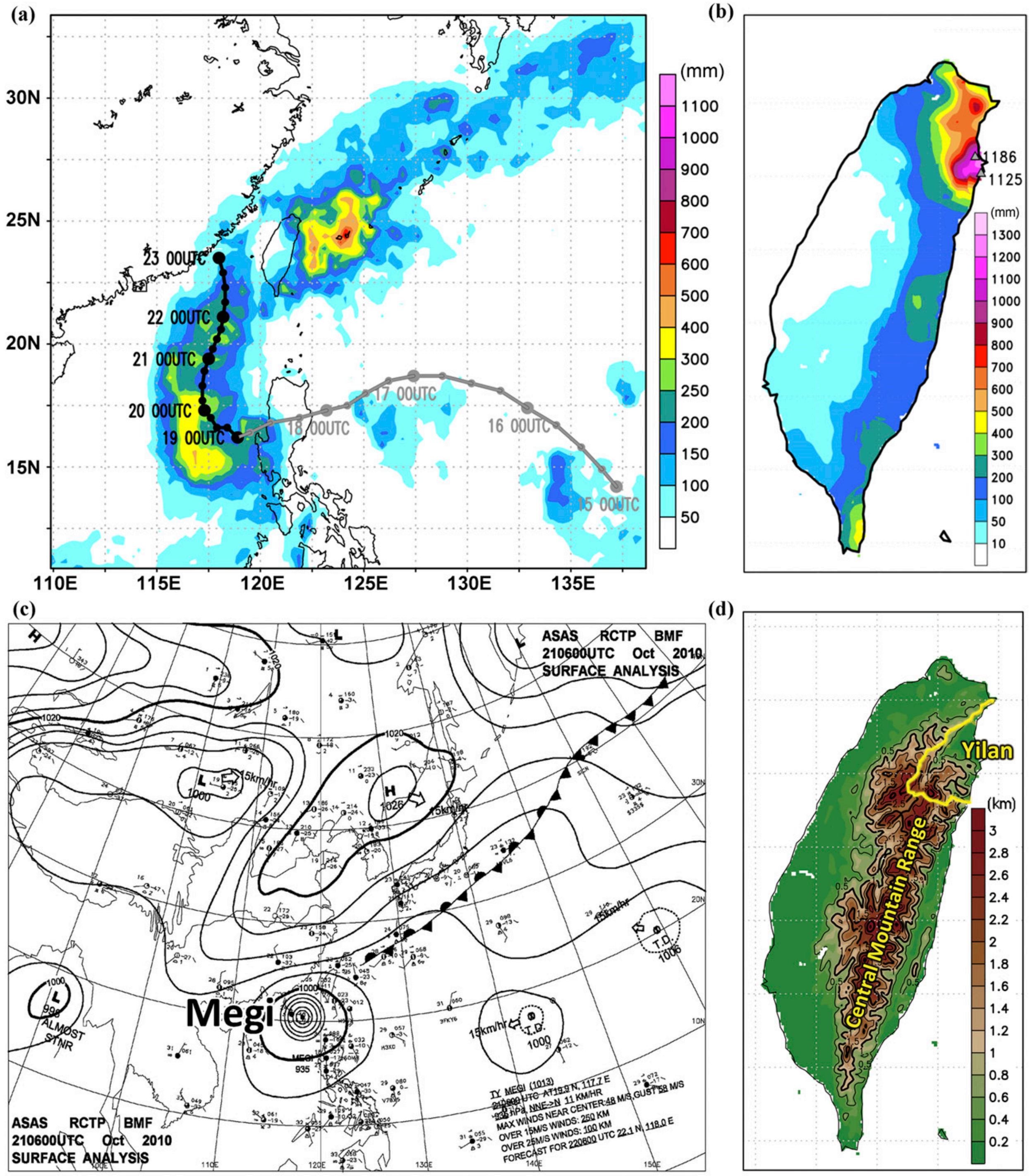

FIG. 1. The 4-day accumulated rainfall (color shaded; mm) from 0000 UTC 19 Oct to 0000 UTC 23 Oct 2010 in (a) the 0.25° resolved, 3-hourly rainfall products derived from the TRMM Multisatellite Precipitation Analysis (TMPA) 3B42 dataset and (b) a Cressman analysis of all automatic rain gauge stations in Taiwan. The best track of Megi from JMA is shown in (a), and the track corresponding to the period of 4-day accumulated rainfall is colored in black. (c) Surface analysis map at 0600 UTC 21 Oct 2010 obtained from the Central Weather Bureau of Taiwan. (d) Terrain height (km) of Taiwan. The yellow line indicates the administrative boundary of Yilan County.

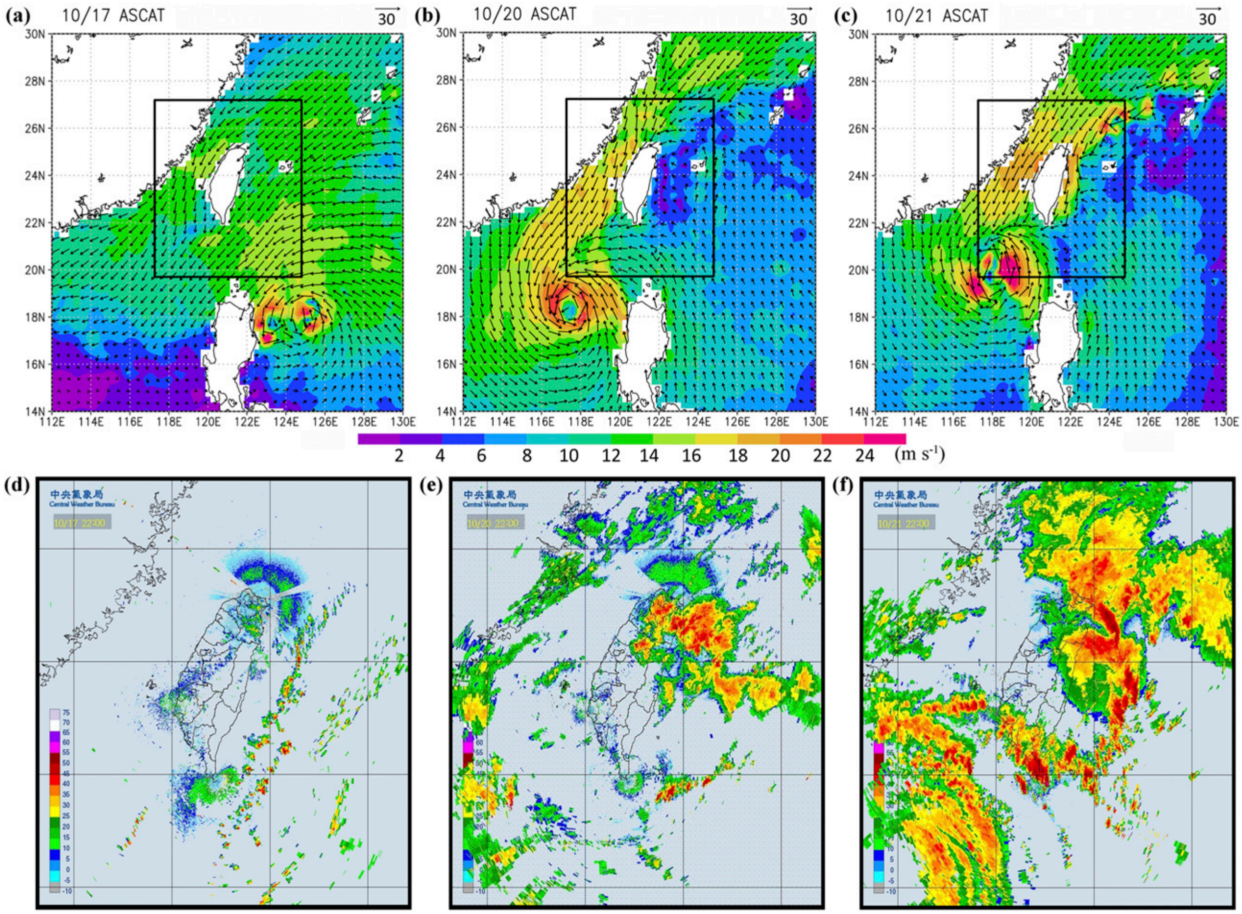

FIG. 2. (top) Daily surface wind fields (wind speed indicated by colored shades; m s^{-1}) estimated from ASCAT retrievals and ECMWF analyses using an objective method (provided by the Asia-Pacific Data-Research Center) on (a) 17, (b) 20, and (c) 21 Oct 2010. (bottom) Radar reflectivity fields provided by the Central Weather Bureau of Taiwan at 1400 UTC (d) 17, (e) 20, and (f) 21 Oct 2010, covering the same areas framed by the black boxes in (a)–(c).

event. Finally, the summary of this study is presented in section 5.

2. An overview of Typhoon Megi

Typhoon Megi formed as a tropical storm on 13 October 2010 to the west-southwest of Guam, reached its peak intensity with a minimum central sea level pressure of 885 hPa at 1800 UTC 17 October when it moved west-northwestward across the WNP at around 4.5 m s^{-1}, and then made landfall at Palanan Bay in northeastern Philippines (i.e., Luzon Island) on 18 October. After Megi left Luzon, it slowed down (with a translation speed of around 2.5 m s^{-1}) and then made a sharp poleward turn at 0000 UTC 20 October, toward Fujian Province of China (Fig. 1a). During and after Megi's sudden recurvature over the South China Sea, in addition to the along-track precipitation produced by the TC circulation itself, excessive precipitation embedded in a bandlike frontal system was observed over northeastern Taiwan and the adjacent seas between 0000 UTC 19 October (when the TC was around 800 km away from northeastern Taiwan) and 0000 UTC 23 October (Figs. 1a,c). The 4-day accumulated rainfall peaked at 1186 mm in Yilan (Figs. 1b,d), and the highest rain rate of 120 mm h^{-1} was recorded on 21 October. Such torrential rainfall led to serious flooding and massive mudslides in the mountainous area in northeastern Taiwan, while a large section of the coastal highway in Yilan collapsed and took more than 26 lives. Before Megi approached Taiwan, the island had already been under the influence of northeasterly monsoon, but with rather light precipitation and low radar reflectivity over Taiwan (Figs. 2a,d). It was not until the northern/northeastern quadrant of Megi's outer circulation reached the eastern coast of Taiwan (after around 19 October) that strong convection and heavy rainfall started to be observed. The daily mean of the Advanced Scatterometer (ASCAT) surface wind field suggests that such precipitation was likely associated with the joint confluent flow of the outer circulation of the recurving TC and the strengthening northeasterly monsoon (Figs. 2b,c). A strong convective system, clearly separated from the TC circulation itself, could be observed in the radar reflectivity imageries during the occurrence of heavy rainfall over northeastern Taiwan from 19 to 23 October (Figs. 2e,f).

Before 0000 UTC 18 October, two days before its recurvature, Megi was forecasted to move westward by most of the operational centers, including the Central Weather Bureau (CWB) of Taiwan, China Meteorological Administration, Japan Meteorological Agency (JMA), Joint Typhoon Warning Center (JTWC), and Hong Kong Observatory. Although the operational ensemble forecasts of the European Centre for Medium-Range Weather Forecasts (ECMWF) began to signal the recurvature in forecasts initialized as early as 1200 UTC 17 October, the significant spread of simulated ensemble tracks indicated that the uncertainty of Megi's recurvature was quite large during the time (Qian et al. 2013). Previous studies have suggested that a TC's sudden poleward track change might be initiated by a binary interaction of the TC and monsoon gyre/trough (e.g., Carr and Elsberry 1995; L. Wu et al. 2013). Several recent studies have identified many possible factors contributing to the significant uncertainty of Megi's sudden recurvature (e.g., Kieu et al. 2012; Qian et al. 2013; Shi et al. 2014; Peng et al. 2014), such as the intensity and size of the simulated Megi, the break of the beltlike subtropical high, the strength of the continental high or the midlatitude trough, and the formation of a low-latitude anticyclonic system southeast of Megi. Nevertheless, there was no consensus on the physical interpretation of the model failure in predicting the recurvature of Megi. In this study, we focus on the QPF related to Megi's remote rainfall effect, and the mechanism behind Megi's sudden recurvature is beyond the scope of the current study.

3. Model configuration and experimental design

The Advanced Research WRF Model (ARW; Skamarock et al. 2008) (version 3.2.1)–based ensemble Kalman filter (EnKF; Evensen 1994, 2003) data assimilation system is used in this study. This system is developed in Meng and Zhang (2008a,b), and, to provide better initial vortex for TC simulations, Wu et al. (2010) further include three TC-related observation operators to the scheme, including the location of TC center, the storm motion vector, and the 700-hPa axisymmetric surface wind profile (derived based on the JMA best track data, the aircraft reports, and the dropwindsonde data). The sizes of the four domains in our experimental setup are 142×100, 166×136, 124×133, and 139×223 grid points, each with a grid spacing of 54, 18, 6, and 2 km, respectively (Fig. 3). The physics parameterization schemes include the WRF single-moment 6-class microphysics scheme (WSM6; Hong and Lim 2006), the Rapid Radiative Transfer Model (RRTM) scheme (Mlawer et al. 1997) for longwave radiation, the Dudhia shortwave scheme (Dudhia 1989) for shortwave radiation, and the Yonsei University (YSU) planetary boundary layer scheme (Hong et al. 2006). The cumulus convection is parameterized with the Grell–Freitas ensemble scheme (Grell and Freitas 2014) only in the outermost domain.

The simulation is initialized based on the National Centers for Environmental Prediction (NCEP) Final Analysis (FNL; $1° \times 1°$) at 0000 UTC 17 October 2010. A total of 36 ensemble members are generated by randomly perturbing the mean analysis in a transformed streamfunction field, as described in Zhang et al. (2006), followed by a 24-h initialization. With valuable aircraft observations [from both Dropwindsonde Observations for Typhoon Surveillance near the Taiwan Region (DOTSTAR) Astra (Wu et al. 2005) and U.S. C-130 flights] collected during the field campaign Impact of Typhoons on the Ocean in the Pacific (ITOP; D'Asaro et al. 2014), the EnKF data assimilation system update cycle is conducted every 1 h during the initialization. A 5-day ensemble simulation is then carried out from 0000 UTC 18 October to 0000 UTC 23 October 2010, which is regarded as the control experiment of this study. In addition, to examine the role of terrain in this remote rainfall event, a supplementary 5-day terrain-removed (TR) experiment is conducted on all the members, in which the land-associated parameters, such as terrain height, land mask, background albedo, and surface skin temperature over Taiwan are set to be the same as those over the surrounding ocean. Our discussion and analyses focus on the 4-day period when the heavy rainfall was observed from 0000 UTC 19 October to 0000 UTC 23 October 2010.

4. Results

Based on the northward-turning angle and 4-day-averaged track error (Fig. 4a), 36 ensemble members associated with different tracks are classified into three categories: the northward (NG, which is closer to the best track with smaller track error), westward (WG, which indicates clear westward track bias) and the remaining group (RG). The northward-turning angle α is defined as

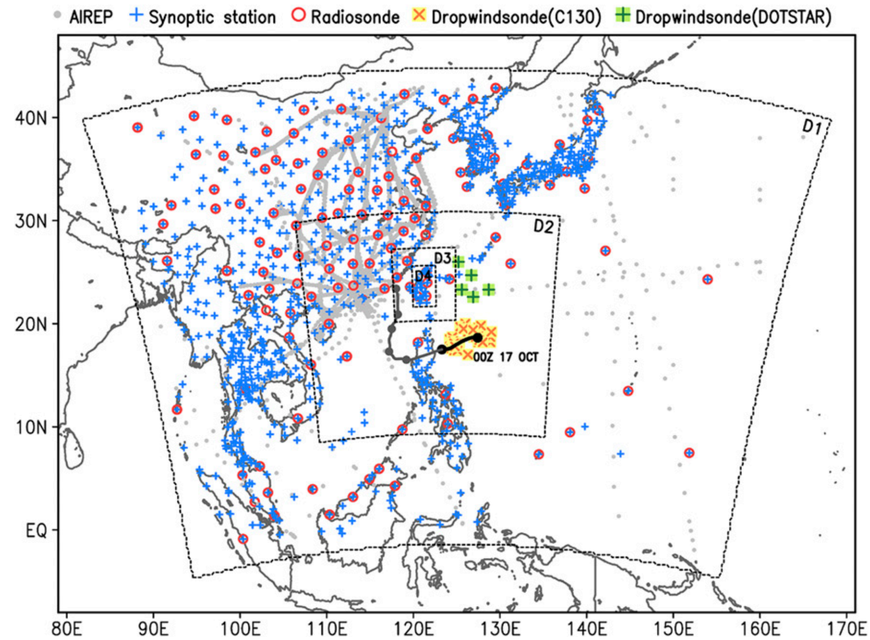

FIG. 3. Horizontal distribution of the data used for initialization, including aircraft reports (AIREP; gray dot), land station data (synoptic station; blue plus sign), radiosondes (red circle), dropwindsonde data collected by DOTSTAR (green square with a plus sign), and C-130 aircraft from the 53rd Air Force Reserve Hurricane Hunter Squadron (yellow square with a "×" sign). The four domains indicated as D1, D2, D3, and D4 represent the model nests with 54-, 18-, 6-, and 2-km horizontal grid spacing, respectively.

$$\alpha = \tan^{-1}\left(\frac{|\mathrm{TC\ lat}_{221800} - \mathrm{TC\ lat}_{180000}|}{|\mathrm{TC\ lon}_{221800} - \mathrm{TC\ lon}_{180000}|}\right), \qquad (1)$$

where TC lat_{ddhhhh} and TC lon_{ddhhhh} represent the location of TC center at the day and time (in UTC) noted in the subscript "ddhhhh." Members with both 4-day-averaged track error below 200 km (above 220 km) and α above 27° (below 26°) are classified under NG (WG). Some exceptional members with extremely slow motion are removed from their original groups, and all the rest of the members are classified under RG, which is not discussed in this study. Note that NG has fewer members (9 members) than WG (23 members). The observational α is 45.5°, while the averaged α for WG and NG is 15.7° and 37.5°, respectively. In addition, a two-sided Student's t test is conducted by calculating the distance between the ensemble-mean locations for NG and WG at a given time, and the result shows that the tracks in NG and WG are significantly different, with 95% confidence after 1700 UTC 18 October 2010. In particular, such early distinct track difference is mainly caused by the longitudinal deviation between these two groups. For the follow-up analyses in this study, a two-sided Student's t test is used to examine the differences in the mean fields between different subgroups.

Figure 5 shows the time evolution of the simulated TC intensity and TC size. Although the ensemble spread in intensity grows larger with time, the simulated intensity is generally consistent with the evolution of the observed storm (we believe that the JMA best track data are more reliable in this case in terms of storm intensity as compared to JTWC, since the former is better consistent with the dropwindsonde data), and there is no significant systematic difference between NG and WG (Fig. 5a). The TC size is defined as the radius of azimuthal-mean $17\ \mathrm{m\,s^{-1}}$ winds in this study. Figure 5b shows that storms in NG are on average smaller than those in WG (thick red and blue lines), and the difference is significant, with 95% confidence starting at around 0000 UTC 19 October, prior to Megi's recurvature. While the poor correspondence between the simulated and observed TC sizes might result from model error, it should be noted that uncertainties still remain in the current, mostly satellite-based, observational TC size estimates.

Figures 6a and 6c show the means of 4-day accumulated rainfall distribution of NG and WG, respectively. Despite large track deviations, the heavy rainfall in Yilan is generally well captured by both NG and WG and is not characterized with statistically significant difference between these two groups. Nevertheless, some variability still exists among

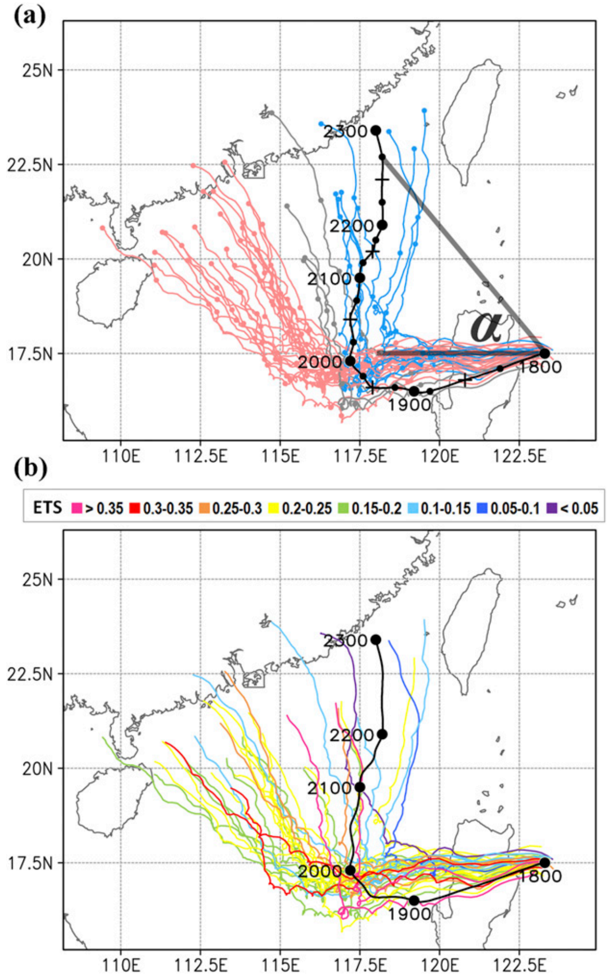

FIG. 4. (a) The best track from JMA (black) and simulated tracks from the control experiment. Lines colored in pink, blue, and gray represent WG, NG, and RG, respectively. The northward-turning angle of the best track is shown by α. (b) As in (a), but colored with their corresponding weighted ETS [ETS at rainfall thresholds above (under) 400 mm have a higher (lower) weight of 0.75 (0.25)].

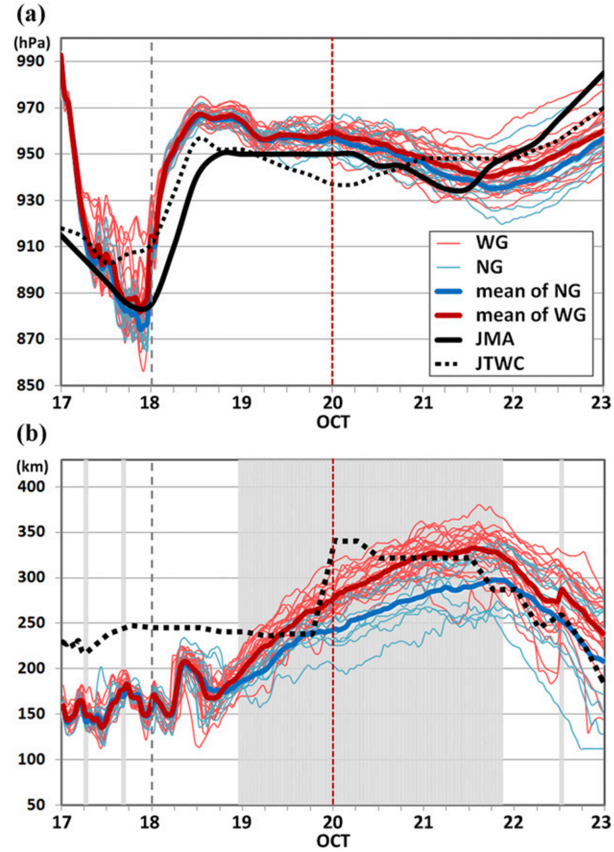

FIG. 5. Time evolutions in the (a) TC intensity (hPa) and (b) TC size (km) of the best track data (solid and dotted black lines for JMA and JTWC data, respectively), ensemble members in WG (thin pink lines) and NG (thin blue lines), and the ensemble means of WG (thick red line) and NG (thick blue line), respectively. Note that the best track data for TC size is derived by taking the average among the analyzed radii of the 34-kt winds in four different quadrants provided by JTWC. The vertical gray (red) dashed line indicates the time when initialization ends (when Megi is observed to make a sudden northward turn). Gray shades represent the time when the difference between NG and WG is statistically significant at the 95% confidence level.

the ensemble members in both the peak rainfall amount over Yilan and the rainfall distribution over the eastern part of Taiwan. NG overestimates the 4-day accumulated precipitation over eastern Taiwan, although the collocated relatively large standard deviation (up to 300 mm) illustrates that such overestimation is characterized with high variability (Fig. 6b). NG's mean precipitation peaks at 1525 mm, which is around 29% higher than the observation. In WG, the mean precipitation pattern is more consistent with the observed rainfall, with a peak value of 1410 mm. Reasons for the above features will be further investigated in the following analyses.

To quantitatively evaluate the QPF skill for each ensemble member, the equitable threat score (ETS; e.g., Schaefer 1990; Black 1994; Chien et al. 2002) is calculated:

$$\mathrm{ETS} = \frac{X - R}{X - R + Y + Z}, \tag{2}$$

where X is the number of hits (i.e., the grid points where a successful forecast of rainfall is made at a given rainfall threshold), while Y and Z are the number of misses and false alarms of the forecast, respectively. The expected hits by a random forecast R are excluded in the measure of model's forecast skill, and R is defined by $R = (X + Y)(X + Z)/(X + Y + W + Z)$, where W is the number of correct rejection (i.e., the number of grid points where both the forecast and observed rainfall amounts are below the given rainfall threshold). ETS is calculated based on the entire landmass of Taiwan, with

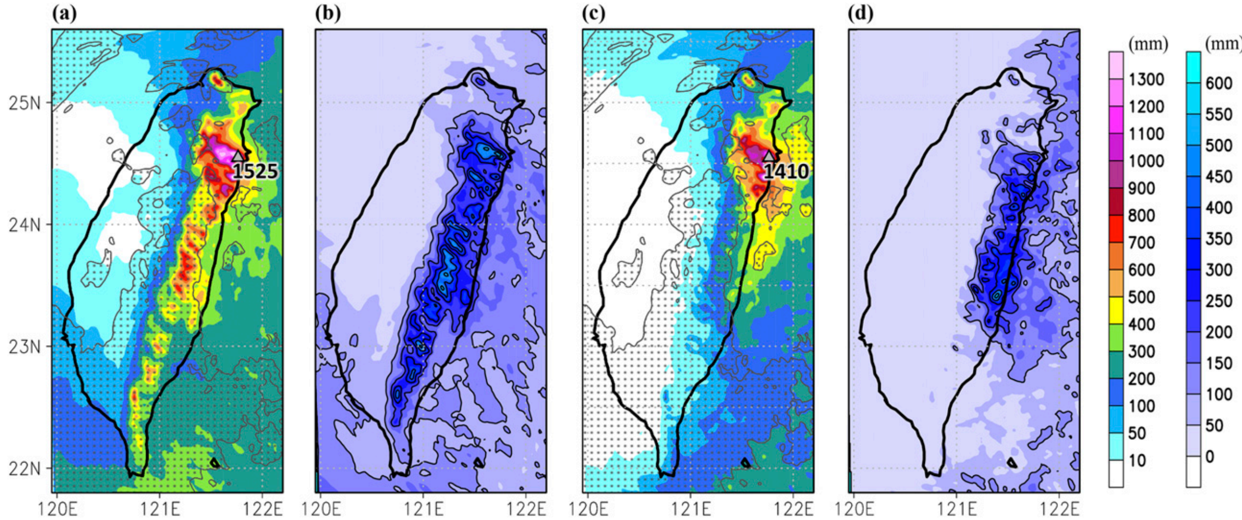

FIG. 6. (a),(c) The 4-day accumulated rainfall (mm) from 0000 UTC 19 Oct to 23 Oct 2010 in the ensemble mean of (a) NG and (c) WG. Dotted areas indicate where the NG − WG difference is statistically significant at the 95% confidence level. (b),(d) The standard deviation of the 4-day accumulated rainfall in (b) NG and (d) WG.

value closer to 1 representing better skill in QPF (i.e., more consistent with the observation).

The result indicates that members with tracks closer to the best track produce more skillful rainfall forecasts only at small rainfall thresholds (e.g., below 400 mm in 4 days) (Fig. 7). Yet there are a few exceptions with small track error that fail to obtain high ETS even at small rainfall thresholds, generally as a result of the rainfall overestimation over eastern Taiwan (not shown) [i.e., on the windward side of the Central Mountain Range (Fig. 1d)]. Such overestimation occurs mainly during the final day of simulation under the TC's direct rainfall effect and is mostly found in NG members with an eastward track bias (i.e., closer to Taiwan), as compared to the best track. The strong easterly upslope flow associated with the proximity of TC circulation induces heavier orographic precipitation. Furthermore, the relation between the accuracy of track forecasts and that of precipitation forecasts is unclear at heavy rainfall thresholds, indicating that the overall

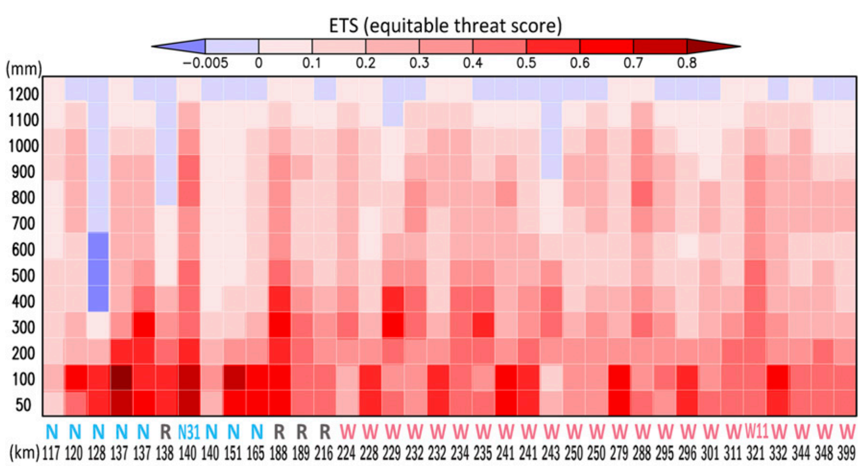

FIG. 7. ETS of the 4-day accumulated rainfall forecasts from 0000 UTC 19 Oct to 0000 UTC 23 Oct 2010 calculated over the entire land area of Taiwan. Ensemble members are arranged in increasing order of track errors from left to right along the abscissa, and the groups they belong to are indicated below (NG, WG, or RG; two representative members, N_m031 and W_m011 that will be further examined are also specified). The 4-day averaged track errors (km) are noted under each member. The ordinate represents the selected rainfall thresholds (mm).

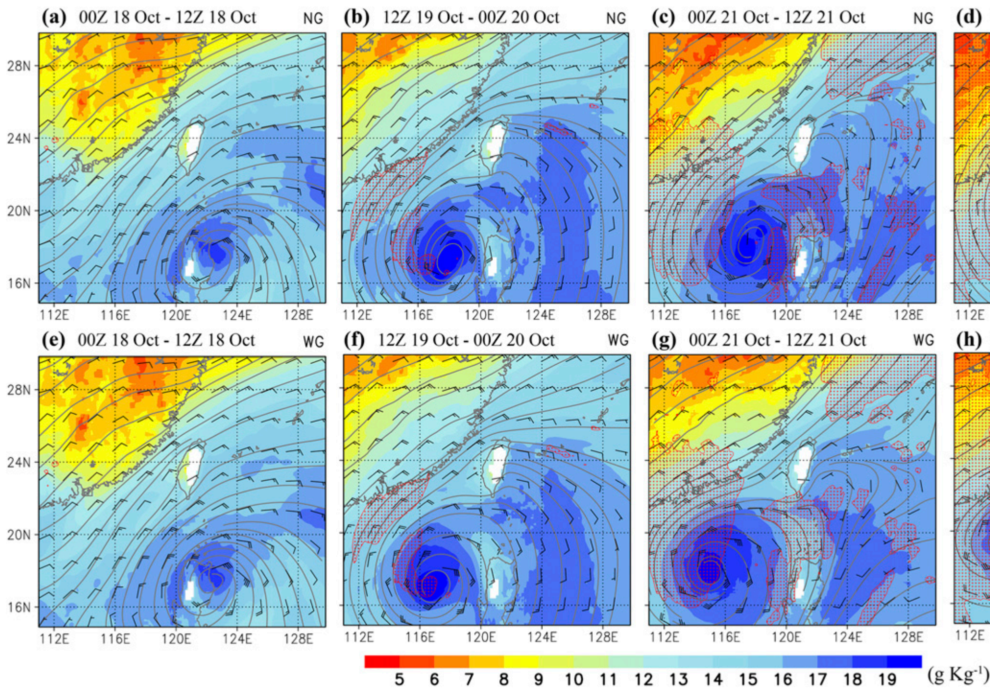

FIG. 8. The 12-h and low-level-averaged (1000–850 hPa) water vapor mixing ratio (color shaded; g kg^{-1}), wind (wind barb; m s^{-1}), and streamlines (gray lines) for the ensemble mean of NG starting at (a) 0000 UTC 18, (b) 1200 UTC 19, (c) 0000 UTC 21, and (d) 0000 UTC 22 Oct 2010. (e)–(h) As in (a)–(d), respectively, but for the ensemble mean of WG. The red dotted pattern indicates the area in which the difference of water vapor mixing ratio between NG and WG is statistically significant at the 95% confidence level.

QPF skill in this remote heavy rainfall event in Yilan is not particularly sensitive to the accuracy of TC tracks (Figs. 7 and 4b).

While the exceptional failure in QPF of some NG is related to the direct impingement of TC circulation on the windward topography, it is of interest to investigate why most of the WG members can also simulate the heavy rains despite their westward track bias and what mechanisms determine the precipitation process in this case. To answer this question, several important mechanisms associated with TC remote rainfall as identified in previous studies will be further examined in the following sections.

a. TC's northward moisture transport

The synoptic water vapor and wind fields in the lower troposphere are first examined (Fig. 8). It is observed that, in both NG and WG, when Megi entered the South China Sea and was about to change its movement from westward to northward, the low-level air with high water vapor mixing ratio is advected northwestward/northward by the TC's outer circulation into the ocean area off the east coast of Taiwan (which is located to the northeast of Megi), thus creating a moisture-laden environment over eastern Taiwan. The northward moisture transport with high water vapor mixing ratio (above 17 g kg^{-1}) and southerly flow is especially important during the period from 19 to 20 October, which can be observed in both groups without a significant difference in moisture field (Figs. 8b,f). Note that the difference in TC tracks between NG and WG is significant with 95% confidence, and the mean longitudinal track difference exceeds 145 km at 0000 UTC 20 October, yet the northeast boundary of the TC circulation in both groups (as indicated with streamlines in Figs. 8b and 8f) is able to reach similar latitude (near 25°N) to the east of Taiwan. It is not until after 21 October, when TCs in WG move farther to the west (Figs. 8c,g), that the moisture difference between NG and WG begins to be statistically significant over a large area. That being said, the mean of mixing ratio remains above 16 g kg^{-1} over the ocean east of Taiwan in WG up to 22 October (Figs. 8g,h). As compared to the moisture field before the TC's approach (Figs. 8a,e), the moistening process over the ocean area east of Taiwan seems to be a general process existing in almost all members regardless of the track bias (Figs. 8d,h).

b. Backward trajectory analyses

To establish the source of the moisture as well as to investigate the roles of the TC's outer circulation and northeasterly monsoon in this remote rainfall event,

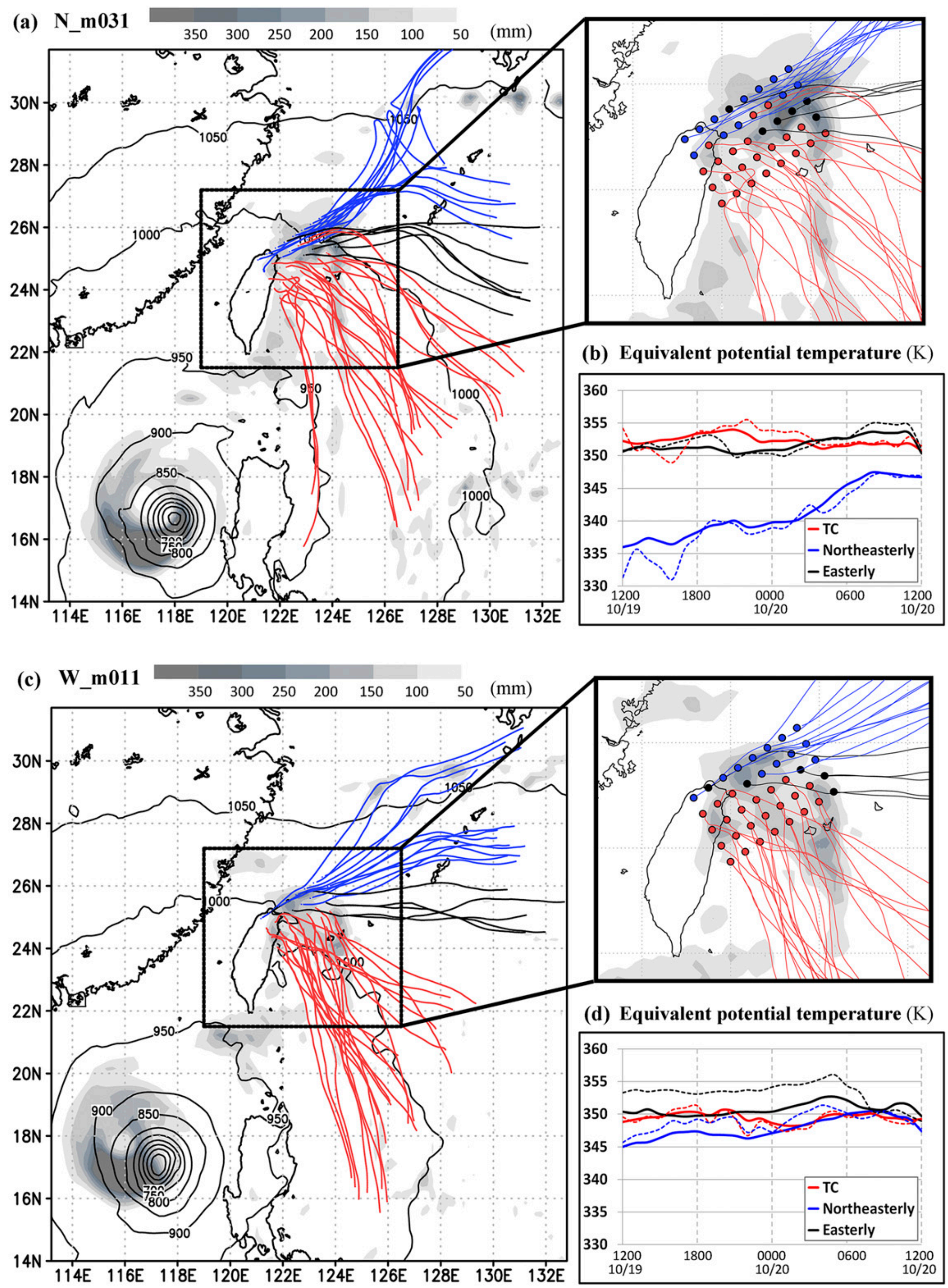

FIG. 9. (a) Forty 24-h backward air parcel trajectories beginning at 900 hPa at 1200 UTC 20 Oct 2010 for the selected member with highest ETS in NG, N_m031, overlaid on the 24-h accumulated rainfall (shaded; mm) from 1200 UTC 19 Oct to 1200 UTC 20 Oct and the 900-hPa geopotential height (contour; m) at 1200 UTC 19 Oct. (b) The 24-h time evolution of equivalent potential temperature (K) averaged over the air parcels originating from the outer circulation of the TC (solid line in red), northeasterly monsoon (solid line in blue), and east of the targeted zone (solid line in black), respectively. The dashed lines represent the median air parcels' equivalent potential temperature (K) in each source region. (c),(d) As in (a),(b), but for the member with the highest ETS in WG, W_m011.

24-h backward air parcel trajectories are computed for the selected member with the highest weighted ETS [ETS at rainfall thresholds above (under) 400 mm have a higher (lower) weight of 0.75 (0.25)] in NG, m031 (here called N_m031). Trajectory analyses are conducted using the Read/Interpolate/Plot (RIP) program (version 4.5) that incorporates an Eulerian integration scheme (Stoelinga 2009). Beginning at 1200 UTC 20 October 2010 (around the time with the highest rainfall rate), 40 air parcels are released at 900 hPa in the rainfall region over and to the northeast of Yilan. Figure 9a shows that these air parcels have generally three source regions: one seems related to the outer circulation of Megi (22 out of the 40 air parcel trajectories), characterized by the counterclockwise trajectories associated with the outer circulation of the TC; another is from east of the targeted rainfall area (6 out of the 40); and the other is from the higher-latitude region (12 out of the 40), advected by the northeasterly monsoon. The confluent flow pattern between the southeasterly flow associated with the TC and the northeasterly monsoon is evident. Time series of both the median and average of the equivalent potential temperature θ_e shows that air parcels from the outer circulation of the TC and the easterly flow transport relatively warmer and moist air with θ_e of around 350 K during the entire period (Fig. 9b). As compared to the other two source regions, the equivalent potential temperature associated with air parcels from the northeasterly monsoon remains the lowest (about 335 K) but becomes higher gradually as air parcels approach the rainfall area. The confluence between the relatively warm, moist (i.e., high θ_e) southeasterly flow associated with Megi and the relatively cool, dry (i.e., low θ_e) northeasterly monsoon appears to set the stage for vigorous convection (see section 4c).

To examine whether the heavy rainfall in WG is also characterized by similar flow patterns, we also conducted the backward air parcel trajectories analysis on another selected member with the highest weighted ETS in WG, m011 (here called W_m011), and the trajectories are similar to that observed in N_m031 (Fig. 9c). While the difference in equivalent potential temperature along trajectories associated with different sources is less distinct in W_m011 than that in N_m031, the northeasterly flow still transports air with slightly lower θ_e as compared to the other two sources. The similarity of trajectories between N_m031 and W_m011 provides an example that is consistent with the previous discussion. Namely, although the tracks between NG and WG are significantly different during this period, the rainfall area northeast of Taiwan is still under the influence of Megi's outer circulation in both NG and WG (Figs. 8b,f). Furthermore, the above results suggest that the TC in WG could play a similar role as in NG (i.e., bringing warm and moist air to the rainfall region) during the early period as long as the TC's outer circulation is large enough to reach the offshore region northeast of Taiwan.

As the TC tracks in N_m031 and W_m011 deviate greatly with time, the backward trajectories for these two members begin to exhibit completely different patterns (Fig. 10). During 1200 UTC 21 October to 1200 UTC 22 October, the source for air near Yilan is mainly to the east and south in N_m031, while in W_m011 the source is generally to the northeast. Note that the different backward trajectory characteristics correspond to different 24-h rainfall distributions across Taiwan, yet both members capture copious rainfall in Yilan during this period (Figs. 10a,b). The rainfall over eastern Taiwan observed in N_m031 suggests a transition from the TC's indirect effect to direct effect on rainfall due to the approach of the storm. Conversely, trajectories in W_m011 imply that the rainfall over northeastern Taiwan is more closely related to the interaction between the northeasterly monsoon and the topography of northeastern Taiwan after 1200 UTC 21 October (Fig. 10b).

c. *Physical mechanisms driving vigorous convection*

First, we focus on the interaction between the northeasterly monsoon and the TC's outer circulation, which is observed in both selected members with the best QPF skill when the heaviest rainfall occurs. The confluence of two different characteristics of air masses (i.e., the relatively warm, moist air transported by the outer circulation of TC (and easterly flow) and the relatively cold, dry air advected by the northeasterly monsoon) is associated with strong low-level frontogenesis in these two selected members (Figs. 11a,c). Conventionally, frontogenesis is defined in terms of the maximum tendency of potential temperature gradient (e.g., the Petterssen frontogenesis equation; Keyser et al. 1986). However, a more common feature of an environment that favors convection in frontal systems in East Asia is the strong gradient of equivalent potential temperature rather than potential temperature. While the former (i.e., the conventional one) can be used to diagnose the thermally induced ageostrophic vertical motion, the latter further implies the generation zone of convective instability and is often more consistent with the observed zone of maximum precipitation for vigorous convective systems in East Asia (e.g., Chen and Chang 1980; Ninomiya 1984; Chen et al. 2000; Yamada et al. 2007). Therefore, frontogenesis in this study is modified to take moisture into consideration (i.e., with potential temperature replaced by equivalent potential temperature) (e.g., Ninomiya 1984, Zhou et al. 2004). Note that we also examined the conventional frontogenesis and derived similar results, despite a reduced magnitude (not shown).

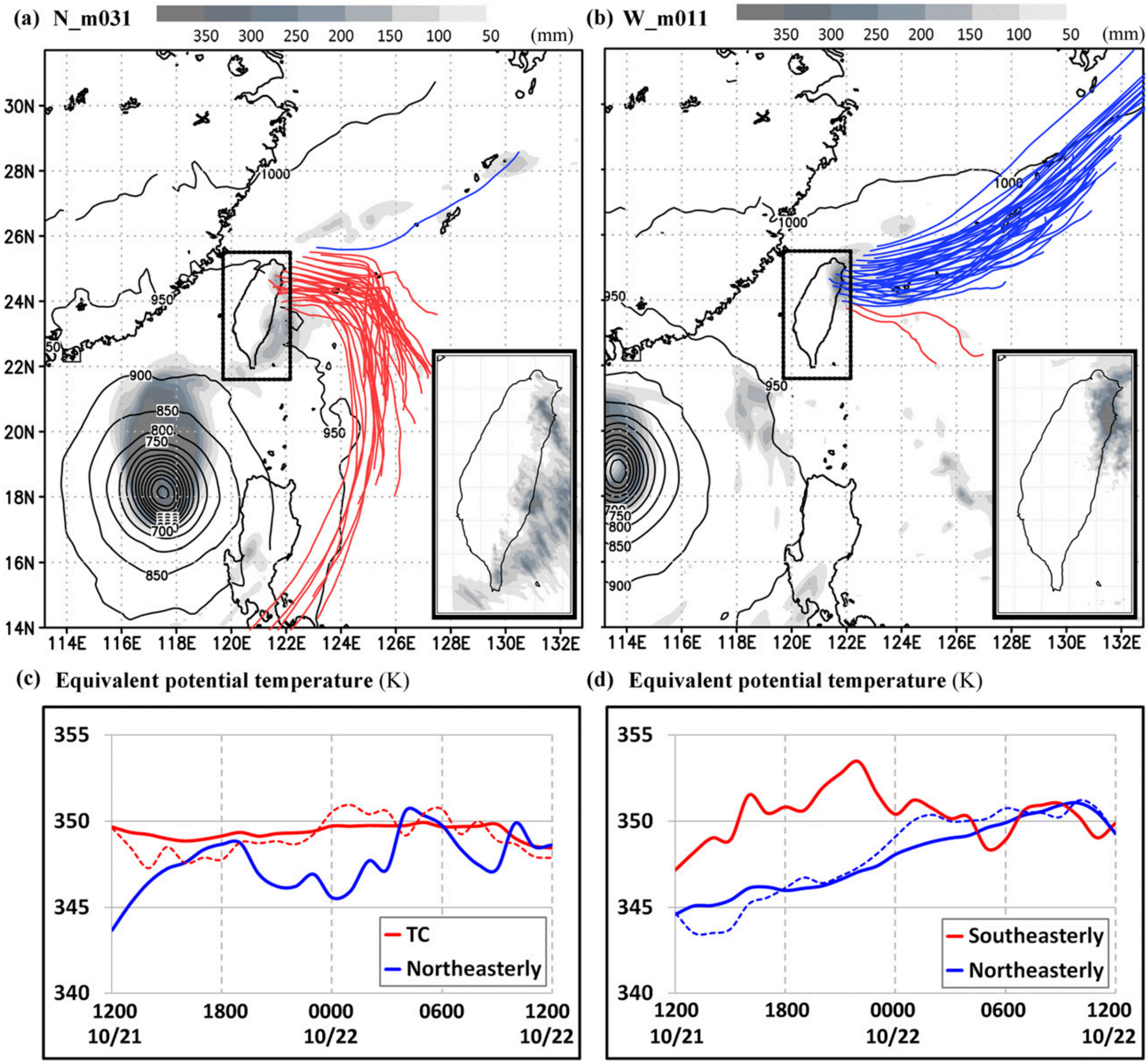

FIG. 10. (a),(c) As in Figs. 9a and 9b, but for the period from 1200 UTC 21 Oct to 1200 UTC 22 Oct. The 24-h accumulated rainfall over Taiwan during this period is shown in the lower-right corner in (a). (b),(d) As in (a),(c), but for W_m011.

Taking the average (averaged along A–B indicated in Figs. 11a and 11c, respectively) of all the cross sections along the southeast–northwest direction (A–A′) over the area with strong frontogenesis, it is shown that, after 18 October, at least one day before remote rainfall begins, the warm, moisture-laden (i.e., high θ_e) air starts to be advected northward to this area. As Megi continues moving westward to the southwest of Taiwan, the poleward transport of high-θ_e air reduces the environmental vertical gradient of equivalent potential temperature ($\partial\theta_e/\partial z$) below 750 hPa, destabilizing the thermodynamic stratification over this area (Figs. 11b,d). When the strongest frontogenesis and heaviest rainfall are observed on 20 October, the low-level horizontal gradient of θ_e is largest at the intersection of the strengthening northeasterly (contours in Figs. 11b and 11d) and southeasterly flow (vectors), and large potential instability is on the warmer side. The time evolution of the cross section along A–A′ shows that the modified frontogenesis slightly shifts horizontally with time and is concentrated near the surface (Fig. 12). The value of frontogenesis peaks above 0.4 K km^{-1} h^{-1} below 950 hPa on 20 October in N_m031 (Figs. 12b,c), and that in W_m011 is slightly weaker. Over the strong frontogenesis region, convective instability is released by convective motions, while the relatively warm and moist southeasterly flow ascends along the lifted

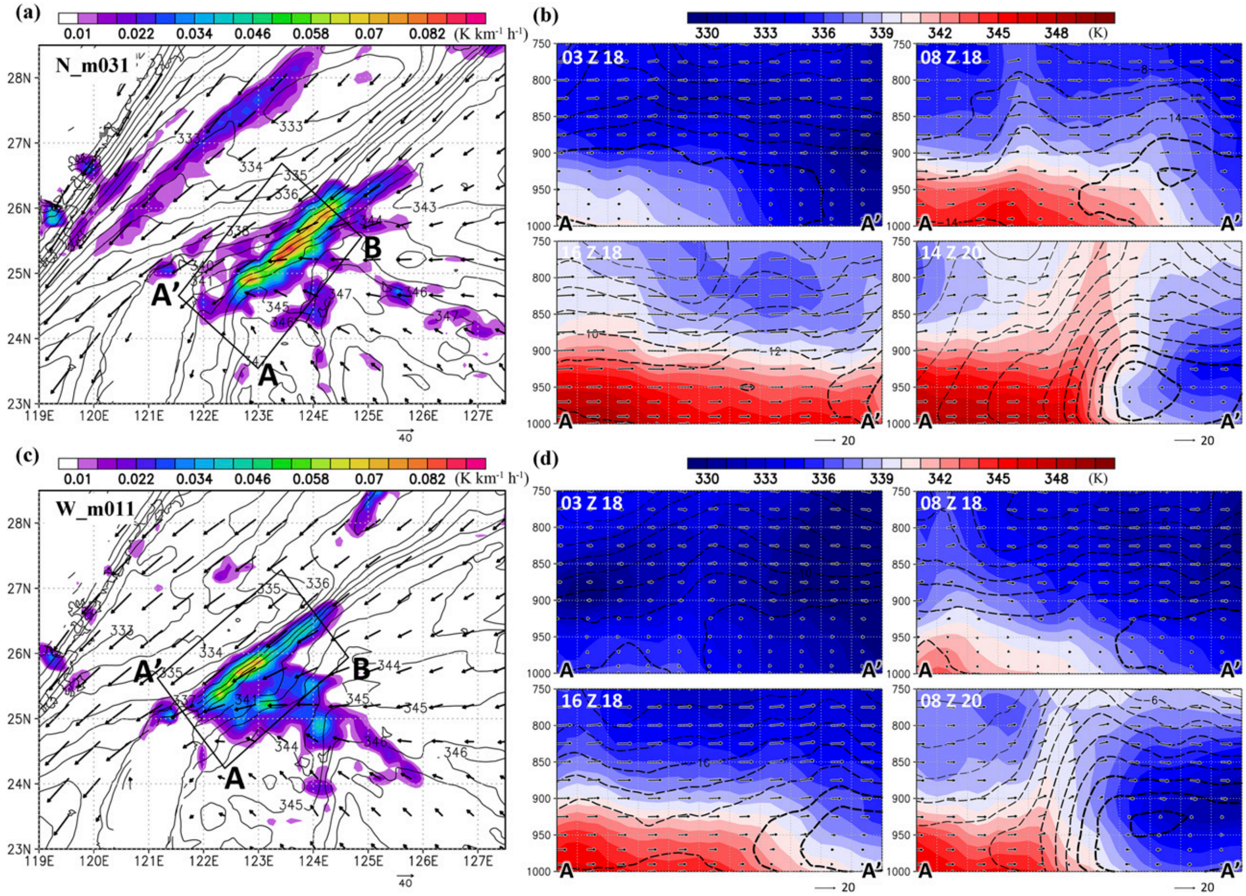

FIG. 11. (a) Daily averaged frontogenesis (shaded; K km^{-1} h^{-1}), wind vectors (m s^{-1}), and equivalent potential temperature (black contours) at 950 hPa for N_m031 on 20 Oct. (b) The time series of the vertical cross section [averaged over the marked area along A–B shown in (a)] of equivalent potential temperature (shaded; K), southeasterly wind (barb; m s^{-1}), and northeasterly wind (dashed black contour; m s^{-1}; solid line represents southwesterly wind). The left-hand side of the cross section represents the southeastern edge along the southeast–northwest direction (A–A′) in (a), while the right-hand side indicates the northwestern edge. (c),(d) As in (a),(b), but for W_m011.

isentropic surfaces (green contours in Fig. 12), which slope upward to the northwest. The spatial scale of the frontogenesis shown in this study is less than 200 km horizontally (in the direction of movement of the warm air) and seldom extends to above 600 hPa.

To systematically investigate whether the frontogenesis is related to track bias, the differences in daily averaged low-level modified frontogenesis between the means of NG and WG are shown in Figs. 13a–d. The result shows that, while frontogenesis is captured in both groups, NG frontogenesis is stronger than that in WG over a large area. On 19 October, NG frontogenesis is more distinct in a small area about 200 km east of Yilan with statistical significance (Fig. 13a). During 20–21 October, NG remains stronger in the magnitude of frontogenesis over several parallel southwest–northeast-oriented zones over the ocean extending to the northeast or east of Taiwan, although not all these areas are characterized by statistically significant differences (Figs. 13b–d). On 22 October, both groups capture much weaker frontogenesis. Although the above result suggests a negative connection between the strength of the frontogenesis and the TC's westward track bias, a wide spatial spread of frontogenesis exists in both NG and WG (frontogenesis frequency observed in WG has similar spatial distribution, but with smaller magnitude as compared to NG; Fig. 14), implying large uncertainty in the predicted location of frontogenesis even for TCs with similar track bias. To sum up, the fact that WG members can still capture the frontogenesis process despite being weaker than NG may help explain why most of them can generally capture the heavy rainfall over Yilan and its adjacent seas. Furthermore, although areas with higher frontogenesis frequency (or stronger mean frontogenesis) do not necessarily correspond to heavier rainfall, NG generally features heavier rainfall over the ocean with

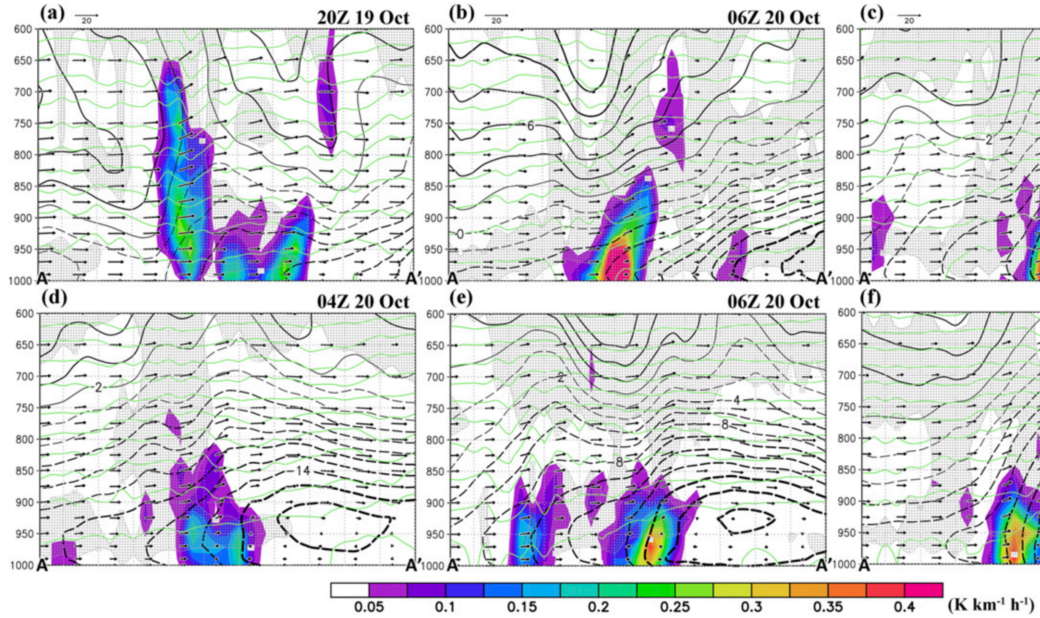

FIG. 12. The vertical cross section (averaged over the marked area along A–B shown in Fig. 11a) of modified Petterssen frontogenesis (shaded; K km^{-1} h^{-1}), southeasterly wind (barb, m s^{-1}), the northeasterly wind (dashed black contour; m s^{-1}; solid line represents southwesterly wind), and isentropic surfaces (green contours; K) for N_m031 at (a) 2000 UTC 19 Oct, (b) 0600 UTC 20 Oct, and (c) 1400 UTC 20 Oct. The dotted pattern indicates the area in which the relative humidity exceeds 95%. (d)–(f) As in (a)–(c), but for W_m011 at (d) 0400, (e) 0600, and (f) 0800 UTC 20 Oct.

stronger frontogenesis (and higher frontogenesis frequency) as compared to WG (Figs. 13a–d, 14). While frontogenesis appears to be necessary for rainfall over ocean, the heavy rains over land (especially Yilan) seem to be not strongly related to the strength of frontogenesis in the adjacent seas (Figs. 14a,b,e,f).

It is of interest to further investigate how the frontogenesis corresponds to the QPF skill over land. A comparison of frontogenesis between two newly defined subgroups with high (hETS) and low weighted ETS (lETS), respectively, is thus examined. The group hETS includes 6 members with weighted ETS in the top 30th percentile, while lETS indicates 7 members having ETS in the bottom 30th percentile. Here, to isolate the mode of precipitation failure, lETS members that fail because they produce too much rainfall over eastern Taiwan are excluded, and only 3 members remain in lETS. Note that the small sample size in lETS may unavoidably affect the robustness of the following analyses as a result of sampling error.

While the difference between hETS and lETS in frontogenesis field shows comparable positive and negative values at different areas, hETS is generally characterized by frontogenesis that is more concentrated just upstream of the heavy precipitation area (Figs. 13e–g). From 19 to 21 October, the mean of hETS features frontogenesis (indicated as the contours in Figs. 13e–g) near the coastal regions to the northeast of Taiwan, while lETS shows either weaker (on 19 October; Fig. 13e) or westward-shifted/-extended frontogenesis that is located to the north of Taiwan (on 20 and 21 October; the negative values in Figs. 13f and 13g). On 22 October, there is almost no frontogenesis in both groups.

The detailed daily evolutions of frontogenesis frequency in relation to the simulated rainfall are described below. On 19 October, the daily precipitation distribution of the mean of lETS is similar to that of hETS, but the former has a slightly larger maximum value over land (Figs. 15a,b). Meanwhile, both groups are characterized with similar daily mean low-level easterly wind flows upstream of Yilan and frontogenesis that is widely distributed over offshore regions north, northeast, and east of Taiwan. The period when lETS fails to obtain high QPF skill over land occurs mainly during 20–21 October (Figs. 15c–f). During this period, although both groups are able to capture the rainfall in areas of frontogenesis frequency over the ocean northeast of Taiwan, the accumulated rainfall over Yilan in lETS is greatly reduced as compared to that in hETS (Figs. 15c–f).

It is therefore suggested that the heavy rainfall over land is more related to the direction of prevailing winds over Yilan and its upstream area, which affects the interaction between the inflow and the topography of Taiwan. While east-southeasterly or southeasterly flows become dominant in lETS, the northeasterly monsoonal flow in hETS extends eastward and southward in the vicinity of Yilan and thus is favorable for triggering

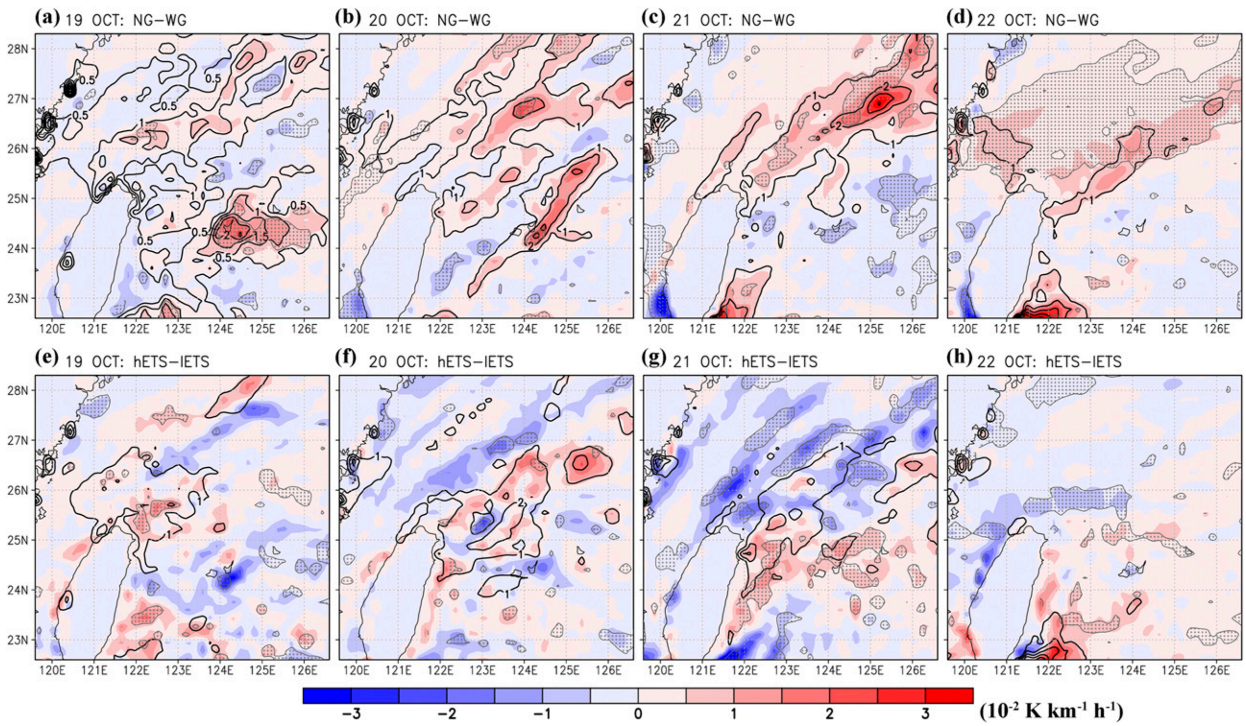

FIG. 13. The difference in daily averaged frontogenesis (shaded; 10^{-2} K km^{-1} h^{-1}) between the means of NG and WG at 990 hPa on (a) 19, (b) 20, (c) 21, and (d) 22 Oct 2010. Black contours are the daily averaged frontogenesis for the mean of NG. The gray dotted pattern indicates the area where the difference between NG and WG is statistically significant at the 95% confidence level. (e)–(h) As in (a)–(d), but for the differences between hETS and lETS. Black contours represent the daily averaged frontogenesis for the mean of hETS.

orographic rainfall with a large impinging angle with respect to the terrain (Figs. 15c–f). The statistical significance level of the difference in northeasterly flow between hETS and lETS is assessed by comparing their northeasterly components of the total wind fields. From Figs. 16e–h, it is shown that the northeasterly monsoonal flow is significantly stronger in hETS than that in lETS starting from 20 October, especially to the northeast of Yilan. In addition, the northeasterly flow difference grows larger with time and is characterized with a wider area by statistical significance. The persistent and strengthening northeasterly component in hETS can also explain why rainfall over land is still observed on 22 October, when the frontogenesis and the rainfall over ocean diminish greatly (Fig. 15g). As to the comparison between NG and WG in northeasterly flow, supportive results are shown. Despite having weaker frontogenesis, the northeasterly flow in WG is able to extend eastward and southward and thus results in a comparable amount of rainfall over Yilan to NG (Figs. 14, 16a–d). In all, the above results indicate that the direction of upstream flow (i.e., the extension of northeasterly wind) plays a vital role in affecting the occurrence of torrential rainfall over land when frontogenesis is present mostly over ocean.

d. Orographic lifting and the TR experiment

While strong frontogenesis is mainly located offshore, the heavy rainfall over the mountainous area in Yilan can be enhanced by both the moisture-laden flow, which advects abundant moisture from frontogenesis area inland, and orographic lifting. Orographic lifting along mountains with steep slopes is a precipitation enhancement mechanism through which conditional and convective instability are released (e.g., Lin 1993; Lin et al. 2001). Precipitation is enhanced when strong horizontal wind convergence occurs over terrain, accompanied by strong forced vertical motion and a highly saturated environment (e.g., Lin et al. 2001; Wu et al. 2002; Jiang 2003). To further elaborate upon this issue, detailed analyses are shown for N_m031, and a TR ensemble experiment is conducted to examine the forecast uncertainty of topographic effects on this heavy rainfall event.

The vertical cross section of horizontal divergence and vertical motion is compared with the hourly precipitation along the axis parallel to the upstream wind over Yilan (black line labeled A–B in Fig. 17a) for N_m031 on 20 October, when the most intense rainfall occurs in the area. The upper panels in Figs. 17b–e show snapshots of horizontal divergence (shaded) and

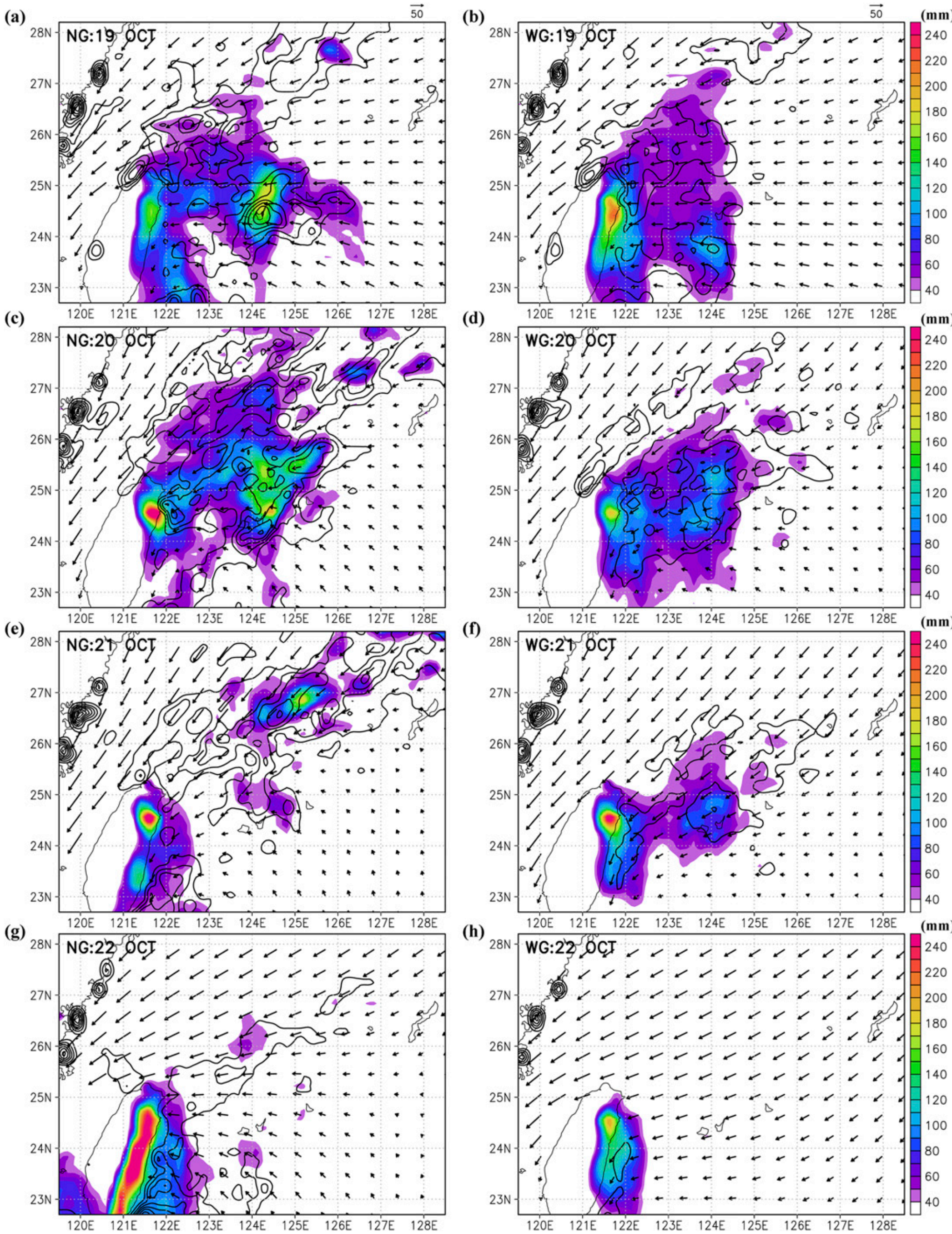

FIG. 14. Daily accumulated rainfall (shaded; mm), 990-hPa wind (vector; $m\ s^{-1}$), and percentage of NG members with daily averaged 990-hPa frontogenesis exceeding $0.025\ K\ km^{-1}\ h^{-1}$ (contour; %; with an interval of 10%) on (a) 19, (c) 20, (e) 21, and (g) 22 Oct 2010. (b),(d),(f),(h) As in (a),(c),(e),(g), but for WG.

the wind fields at some given time during 20 October, while the bottom panels represent the hourly accumulated precipitation at each grid point along A–B starting from 30 min prior to each given time. The locations of precipitation well match the areas of strong horizontal convergence and the associated vertical motion. In addition, 90% of the strong vertical motions (derived in the innermost domain from the WRF Model) at the lowest model level can be estimated by the orographically induced vertical motion, $W_{oro} = \mathbf{u} \cdot \nabla h$ (where $\mathbf{u}$ is the wind vector and h is the terrain height; Lin et al. 2001), with a coefficient of

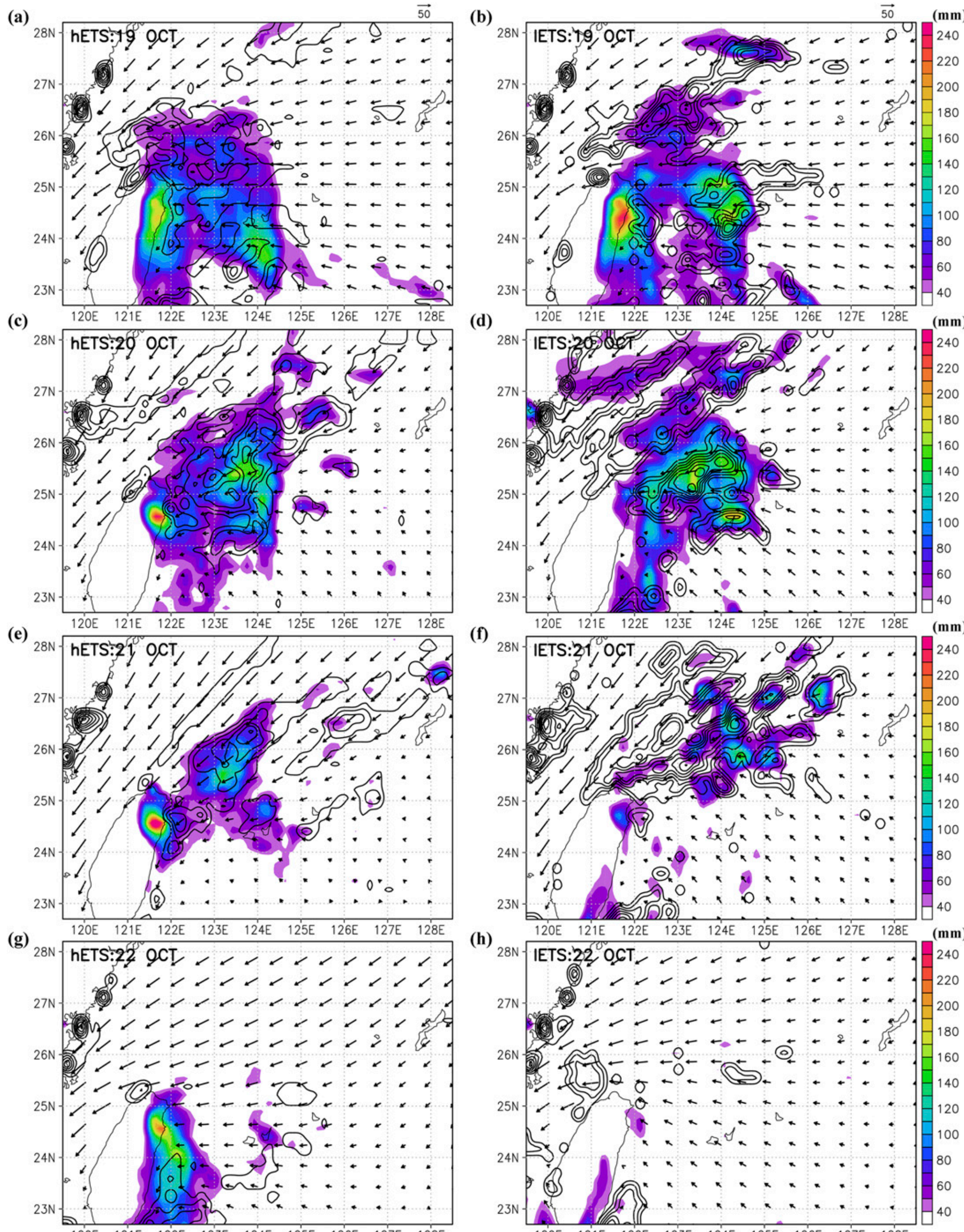

FIG. 15. As in Fig. 14, but for hETS and lETS, respectively.

determination R^2 of the regression as high as 0.71 over northeastern Taiwan (the calculation is conducted over the landmass north of 24.16°N and east of 121.1°E). From the time evolution of the horizontal divergence and the wind field, it is also shown that an initially weak/moderate convection (Fig. 17b) is strengthened greatly through orographic lifting when it encounters the mountain (Figs. 17c,d). When the low-level (approximately below 1.5 km) inflow intensifies, the location of strong convergence and maximum precipitation shifts downstream toward the mountain peak correspondingly (Fig. 17e). The highest rain rate is recorded at 100 mm h^{-1}, and the instantaneous maximum wind peaks at about 7 m s^{-1} during the period (Fig. 17d).

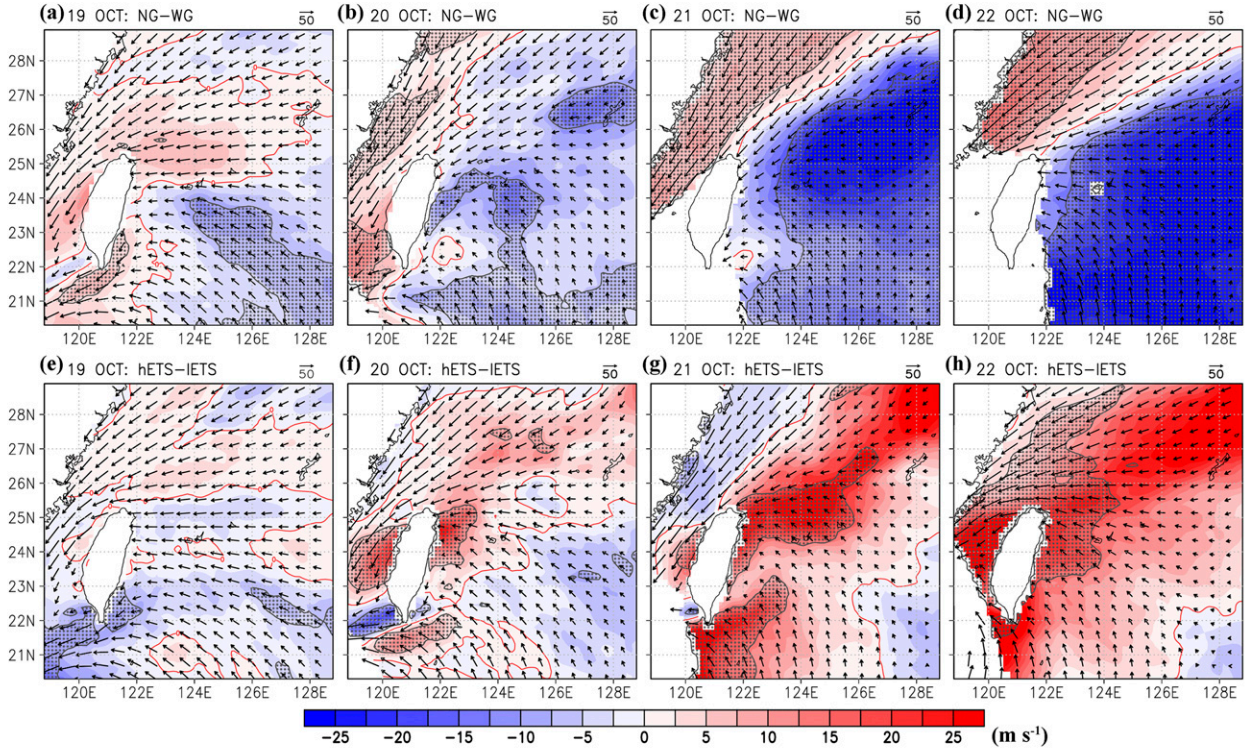

FIG. 16. The difference in daily averaged northwesterly wind (only the northeasterly component of total wind field is compared) between the means of NG and WG (shaded; m s^{-1}) at 990 hPa on (a) 19, (b) 20, (c) 21, and (d) 22 Oct. The vectors denote the total wind at 990 hPa for the mean of WG (m s^{-1}). Gray dotted regions indicate where the difference is statistically significant at the 95% confidence level. (e)–(h) As in (a)–(d), but for hETS and lETS. The vectors denote the total wind at 990 hPa for the mean of lETS.

The impact of orographic lifting on this remote rainfall event is further examined based on the TR experiment. All simulated tracks of Megi in TR deviate slightly westward from those of the control experiment after the TC's northward recurvature at 0000 UTC 20 October (not shown), which is likely related to the enhanced easterly steering flow when the topographic blocking is removed. Furthermore, the simulated TC intensity for each TR experiment is similar to the corresponding control experiment. Without the topography that blocks and lifts moisture on the windward side of the mountains, almost all members in TR show evenly distributed rainfall patterns with the maximum 4-day accumulated precipitation reduced by more than 80% as compared to the control experiment (in domain 4 with 2-km horizontal spacing; figure not shown). To examine the difference of the larger-scale rainfall distribution, the ensemble means of the simulated 4-day accumulated rainfall in the control and TR experiments with resolution of 18 km (in domain 2) are compared in Fig. 18. It has been shown that the simulated rainfall is reduced when the horizontal resolution is not high enough to accurately represent the topography (e.g., Wu et al. 2002; Yang et al. 2008; Zhang et al. 2010; C.-C. Wu et al. 2013). Therefore, rainfall amounts shown in domain 2 are actually smaller than those in domain 4, and the features in Fig. 18 can only be qualitatively analyzed. When the Taiwan topography is removed, the heavy precipitation at Yilan and the coastal areas is greatly reduced by statistical significance (Fig. 18c), but the distant precipitation over the ocean northeast of Yilan (with maximum located near 24.5°N, 124°E) can still be identified with almost unchanged magnitude in maximum rainfall. In all, the finding in TR suggests two points: 1) the heavy rainfall over the ocean is mainly attributed to the interaction between the northeasterly monsoon and Megi's outer circulation (i.e., lifting mechanism that is linked to frontogenesis between air masses with two distinguishing characteristics) as shown in section 4c; and 2) the occurrence of torrential rainfall over land requires orographic lifting to enhance vigorous vertical motion over mountains.

5. Summary

Quantitative precipitation forecasting of typhoon-induced rainfall over Taiwan has always been a challenging task,

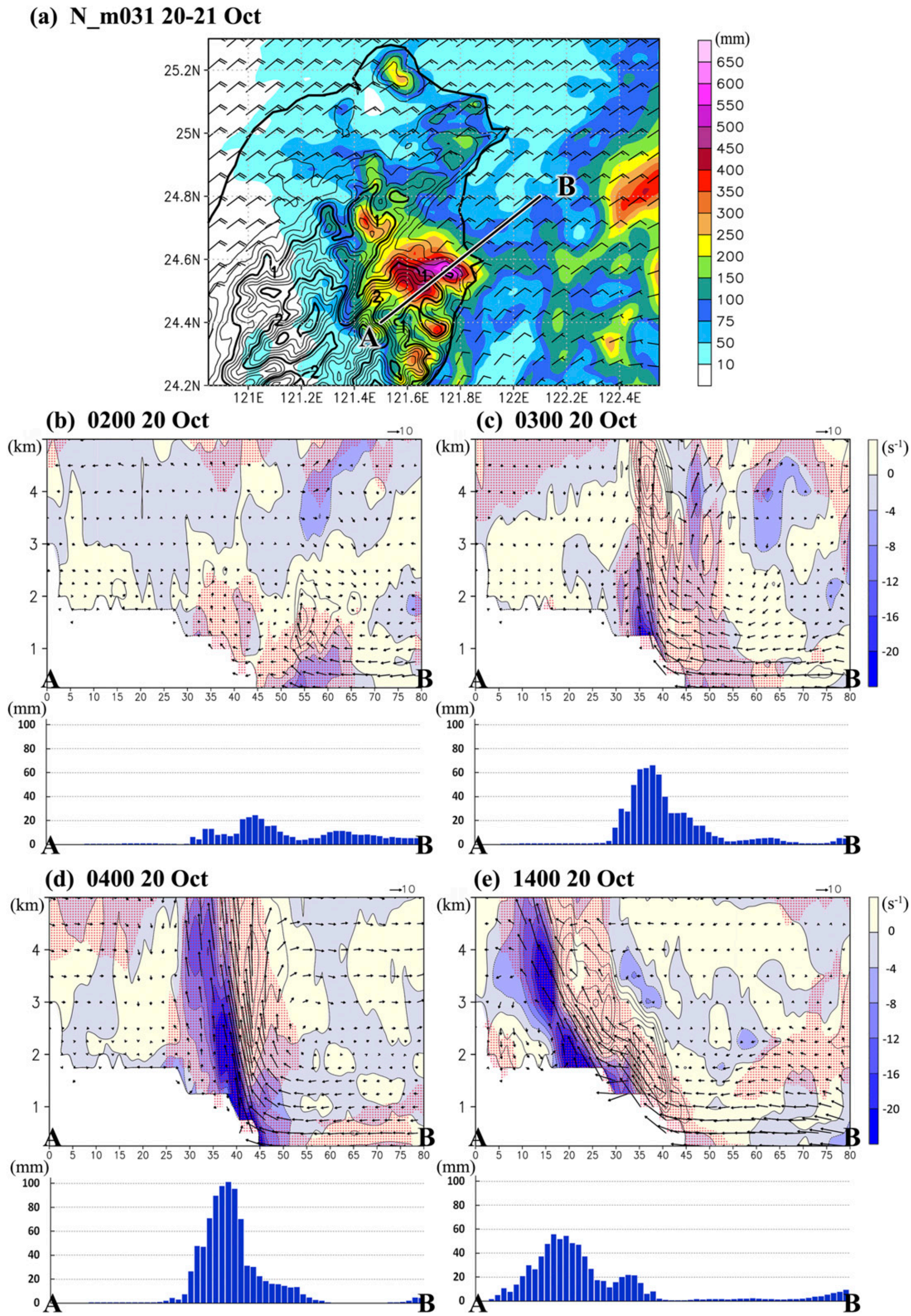

FIG. 17. (a) Daily accumulated rainfall (shaded; mm) and 950-hPa wind vector (m s^{-1}) in N_m031 on 20 Oct. (b)–(e) (top) The cross sections of horizontal divergence (color shaded; s^{-1}) and wind vector (m s^{-1}; vertical wind is multiplied by a factor of 10) along the black line labeled A–B in (a) at (b) 0200, (c) 0300, (d) 0400, and (e) 1400 UTC 20 Oct. Areas in white represent the terrain. The region with relative humidity above 99% is marked by red dots. (b)–(e) (bottom) The corresponding hourly accumulated rainfall (bar; mm) at each grid point along A–B starting from 30 min prior to each given time.

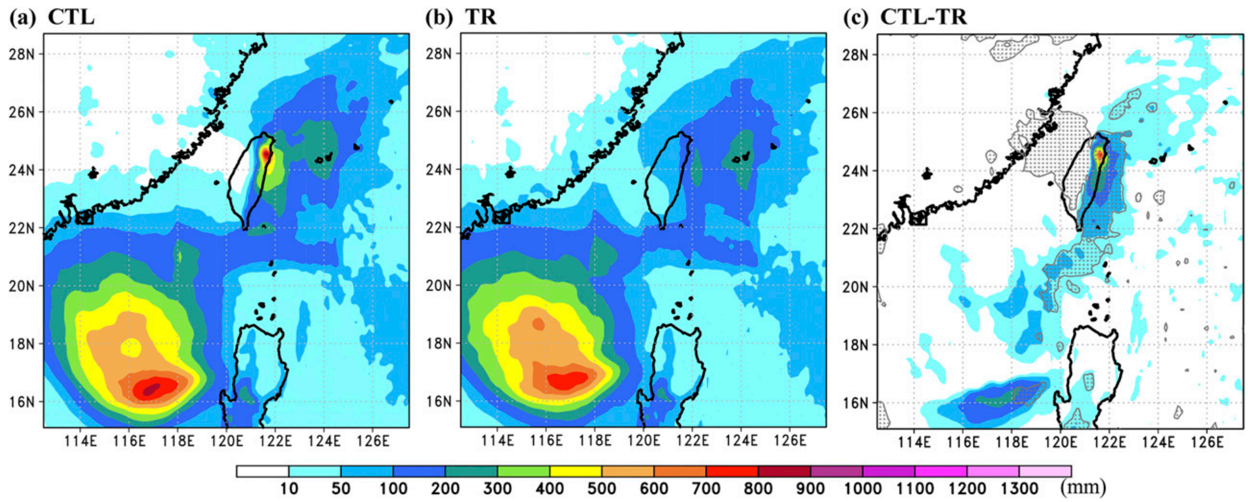

FIG. 18. The mean of 4-day accumulated rainfall (mm) in (a) the control experiment, (b) the TR experiment, and (c) the difference between control and TR from 0000 UTC 19 Oct to 0000 UTC 23 Oct 2010. Dotted areas in (c) indicate where the control − TR difference is statistically significant at the 95% confidence level.

especially for cases with high uncertainty in track forecasts. A case study has been conducted on Typhoon Megi (2010), which features high uncertainties in both its track prediction and the associated heavy rainfall in a distant area over northeastern Taiwan and its adjacent seas during 0000 UTC 19–23 October. The mechanisms for and the variability with this rainfall event are investigated by conducting an ensemble simulation.

In contrast to previous typhoon-rainfall studies for landfalling cases, the quantitative evaluation of the precipitation forecast based on the equitable threat score (ETS) shows that the performance of rainfall forecasts in this remote rainfall event is not particularly sensitive to TC track, especially for high accumulated rainfall thresholds (e.g., above 400 mm in 4 days). When Megi is about to recurve over the South China Sea, its outer circulation helps transport relatively warm air with high water vapor mixing ratio northward, establishing a moist, potentially unstable environment that is favorable for convection over the ocean to the east and northeast of Taiwan. Such an environment conducive to rainfall exists in most of the members, including in the group with westward track bias. Under such favorable conditions, the southeasterly flow (with high θ_e) associated with Megi's outer circulation encounters the northeasterly monsoon (with low θ_e) to the northeast of Yilan, leading to vigorous convection in association with strong low-level frontogenesis over the offshore and nearshore areas of northeastern Taiwan. Over the frontogenesis region, the southeasterly flow ascends along the lifted isentropic surfaces, which slope poleward with height. While a negative relationship is suggested between the strength of the frontogenesis and the TC's westward track bias, the wide spatial spread of frontogenesis among all members suggests a great challenge to accurately predict the location of the frontogenesis even for TCs with similar tracks. Analysis is also conducted to understand how frontogenesis corresponds to the rainfall simulation. While rainfall over ocean can be mostly well explained by the frontogenesis process, the connection between frontogenesis and QPF skill over land is less significant. Despite a lack of statistically significant difference, members with high ETS (hETS) generally have frontogenesis closer to the coastal area to the northeast of Taiwan, while members with low ETS (lETS) on average feature either weaker or eastward-shifted/-extended frontogenesis.

Most importantly, it is found that the direction of prevailing wind has a great impact on the rainfall amount over land as a result of the interaction with inflow and the topography. The hETS group has significantly stronger low-level northeasterly flow upstream of Yilan than the lETS group. If the northeasterly monsoon extends eastward and southward toward the coastal area east of Taiwan, the prevailing northeasterly wind can further advect the moisture inland, while the steep mountains located to the south-southwest of Yilan induce strong orographic lifting. In other words, for upstream flow with larger impinging angle (i.e., more perpendicular to the steep windward mountains), stronger vertical motion as well as orographic rainfall can be induced through orographic lifting, as compared to flows with smaller impinging angle. Therefore, even under similar conditions with vigorous convection (associated with frontogenesis) over upstream ocean, the members with northeasterly flow near Yilan can better simulate the heavy orographic rainfall compared to other members with southeasterly flow. The above results suggest that the variability/uncertainty of the low-level upstream flow over the coastal area (i.e., the impinging angle relative to the windward mountain barriers), partly affected by the strength and range of monsoon system, can lead to diverse rainfall patterns and amounts over northeastern Taiwan. Furthermore, in the terrain-removed (TR) experiment, the reduction of peak rainfall in Taiwan by more than 80% indicates that the topographic lifting plays a dominant role in enhancing the heavy orographic rainfall at Yilan among all the ensemble members in this remote rainfall event.

In all, this study not only identifies several favorable mechanisms leading to the heavy remote rainfall at Yilan and its adjacent seas, but it also highlights that the uncertainty of a TC's remote rainfall processes can be increased as a result of the complicated TC–monsoon–terrain interaction. Contributing factors to the uncertainty of remote rainfall simulation include the variation of TC track (which might affect the northward moisture transport by the TC's outer circulation, although that does not seem to have a large impact on the remote rainfall in this study), as well as the strength and extension of the monsoon system, all of which can further affect the location and magnitude of a mesoscale lifting mechanism (i.e., frontogenesis). Even when the above favorable conditions are met over the ocean offshore, the direction of the prevailing wind over Yilan and its upstream area relative to the orientation of the mountains is as important in determining whether the torrential rainfall will be triggered. While the above contributing factors are identified in the current study, it should be noted that one of the caveats in this study is the lack of sample sizes. Therefore, further follow-up work remains to be carried out with larger sample sizes to examine the robustness of these results as well as to investigate the dynamical processes and the source of errors governing the variability of these contributing factors. Since a TC's remote/indirect rainfall effect may result in unexpected weather hazards, the physical insights obtained in this study can be applied to assess the likelihood of such an extreme weather event in real-time forecasts, especially for the cases with high uncertainty in storm-track forecasts.

Acknowledgments. This study is supported by the Ministry of Science and Technology of Taiwan through Grant MOST 103-2628-M-002-004 and the Office of Naval Research through Grant ONR-102E32063. Valuable comments from the editor and three anonymous reviewers that helped improve the quality of the manuscript are highly appreciated.

REFERENCES

Atallah, E. H., and L. F. Bosart, 2003: The extratropical transition and precipitation distribution of Hurricane Floyd (1999). *Mon. Wea. Rev.*, **131**, 1063–1081, doi:10.1175/1520-0493(2003)131<1063:TETAPD>2.0.CO;2.

Black, T. L., 1994: The new NMC mesoscale Eta Model: Description and forecast examples. *Wea. Forecasting*, **9**, 265–278, doi:10.1175/1520-0434(1994)009<0265:TNNMEM>2.0.CO;2.

Carr, L. E., and R. L. Elsberry, 1995: Monsoonal interactions leading to sudden tropical cyclone track changes. *Mon. Wea. Rev.*, **123**, 265–290, doi:10.1175/1520-0493(1995)123<0265:MILTST>2.0.CO;2.

Chang, C.-P., T.-C. Yeh, and J. M. Chen, 1993: Effects of terrain on the surface structure of typhoons over Taiwan. *Mon. Wea. Rev.*, **121**, 734–752, doi:10.1175/1520-0493(1993)121<0734:EOTOTS>2.0.CO;2.

Chen, S.-J., W. Wang, K.-H. Lau, Q.-H. Zhang, and Y.-S. Chung, 2000: Mesoscale convective systems along the Meiyu front in a numerical model. *Meteor. Atmos. Phys.*, **75**, 149–160, doi:10.1007/s007030070002.

Chen, T.-J. G., and C.-P. Chang, 1980: The structure and vorticity budget of an early summer monsoon trough (Mei-Yu) over southeastern China and Japan. *Mon. Wea. Rev.*, **108**, 942–953, doi:10.1175/1520-0493(1980)108<0942:TSAVBO>2.0.CO;2.

Chien, F.-C., and H.-C. Kuo, 2011: On the extreme rainfall of Typhoon Morakot (2009). *J. Geophys. Res.*, **116**, D05104, doi:10.1029/2010JD015092.

——, Y.-H. Kuo, and M.-J. Yang, 2002: Precipitation forecast of MM5 in the Taiwan area during the 1998 Mei-yu season. *Wea. Forecasting*, **17**, 739–754, doi:10.1175/1520-0434(2002)017<0739:PFOMIT>2.0.CO;2.

——, Y.-C. Liu, and C.-S. Lee, 2008: Heavy rainfall and southwesterly flow after the leaving of Typhoon Mindulle (2004) from Taiwan. *J. Meteor. Soc. Japan*, **86**, 17–41, doi:10.2151/jmsj.86.17.

Colle, B. A., 2003: Numerical simulations of the extratropical transition of Floyd (1999): Structural evolution and responsible mechanisms for the heavy rainfall over the northeast United States. *Mon. Wea. Rev.*, **131**, 2905–2926, doi:10.1175/1520-0493(2003)131<2905:NSOTET>2.0.CO;2.

Cote, M. R., 2007: Predecessor rain events in advance of tropical cyclones. M.S. thesis, Dept. of Atmospheric and Environmental Sciences, University at Albany, State University of New York, 200 pp. [Available online at http://cstar.cestm.albany.edu/CAP_Projects/Project10/index.htm.]

D'Asaro, E. A., and Coauthors, 2014: Impact of typhoons on the ocean in the Pacific. *Bull. Amer. Meteor. Soc.*, **95**, 1405–1418, doi:10.1175/BAMS-D-12-00104.1.

Dudhia, J., 1989: Numerical study of convection observed during the Winter Monsoon Experiment using a mesoscale two-dimensional model. *J. Atmos. Sci.*, **46**, 3077–3107, doi:10.1175/1520-0469(1989)046<3077:NSOCOD>2.0.CO;2.

Evensen, G., 1994: Sequential data assimilation with a nonlinear quasi-geostrophic model using Monte Carlo methods to forecast error statistics. *J. Geophys. Res.*, **99**, 10 143–10 162, doi:10.1029/94JC00572.

——, 2003: The ensemble Kalman filter: Theoretical formulation and practical implementation. *Ocean Dyn.*, **53**, 343–367, doi:10.1007/s10236-003-0036-9.

Fang, X., and Y.-H. Kuo, 2013: Improving ensemble-based quantitative precipitation forecasts for topography-enhanced typhoon heavy rainfall over Taiwan with a modified probability-matching technique. *Mon. Wea. Rev.*, **141**, 3908–3932, doi:10.1175/MWR-D-13-00012.1.

——, ——, and A. Wang, 2011: The impacts of Taiwan topography on the predictability of Typhoon Morakot's record-breaking rainfall: A high-resolution ensemble simulation. *Wea. Forecasting*, **26**, 613–633, doi:10.1175/WAF-D-10-05020.1.

Galarneau, T. J., L. F. Bosart, and R. S. Schumacher, 2010: Predecessor rain events ahead of tropical cyclones. *Mon. Wea. Rev.*, **138**, 3272–3297, doi:10.1175/2010MWR3243.1.

Grell, G. A., and S. R. Freitas, 2014: A scale and aerosol aware stochastic convective parameterization for weather and air quality modeling. *Atmos. Chem. Phys.*, **14**, 5233–5250, doi:10.5194/acp-14-5233-2014.

Hong, S.-Y., and J.-O. J. Lim, 2006: The WRF Single-Moment 6-Class Microphysics Scheme (WSM6). *J. Korean Meteor. Soc.*, **42**, 129–151.

——, Y. Noh, and J. Dudhia, 2006: A new vertical diffusion package with an explicit treatment of entrainment processes. *Mon. Wea. Rev.*, **134**, 2318–2341, doi:10.1175/MWR3199.1.

Huang, Y.-C., and Y.-L. Lin, 2014: A study on the structure and precipitation of Morakot (2009) induced by the Central Mountain Range of Taiwan. *Meteor. Atmos. Phys.*, **123**, 115–141, doi:10.1007/s00703-013-0290-4.

Huang, Y.-H., C.-C. Wu, and Y. Wang, 2011: The influence of island topography on typhoon track deflection. *Mon. Wea. Rev.*, **139**, 1708–1727, doi:10.1175/2011MWR3560.1.

Jiang, Q., 2003: Moist dynamics and orographic precipitation. *Tellus*, **55A**, 301–316, doi:10.1034/j.1600-0870.2003.00025.x.

Jones, S. C., and Coauthors, 2003: The extratropical transition of tropical cyclones: Forecast challenges, current understanding, and future directions. *Wea. Forecasting*, **18**, 1052–1092, doi:10.1175/1520-0434(2003)018<1052:TETOTC>2.0.CO;2.

Keyser, D., M. J. Pecnick, and M. A. Shapiro, 1986: Diagnosis of the role of vertical deformation in a two-dimensional primitive equation model of upper-level frontogenesis. *J. Atmos. Sci.*, **43**, 839–850, doi:10.1175/1520-0469(1986)043<0839:DOTROV>2.0.CO;2.

Kieu, C. Q., N. M. Truong, H. T. Mai, and T. Ngo-Duc, 2012: Sensitivity of the track and intensity forecasts of Typhoon Megi (2010) to satellite-derived atmospheric motion vectors with the ensemble Kalman filter. *J. Atmos. Oceanic Technol.*, **29**, 1794–1810, doi:10.1175/JTECH-D-12-00020.1.

Lee, C.-S., Y.-C. Liu, and F.-C. Chien, 2008: The secondary low and heavy rainfall associated with Typhoon Mindulle (2004). *Mon. Wea. Rev.*, **136**, 1260–1283, doi:10.1175/2007MWR2069.1.

Lin, Y.-L., 1993: Orographic effects on airflow and mesoscale weather systems over Taiwan. *Terr. Atmos. Oceanic Sci.*, **4**, 381–420.

——, S. Chiao, T.-A. Wang, M. L. Kaplan, and R. P. Weglarz, 2001: Some common ingredients for heavy orographic rainfall. *Wea. Forecasting*, **16**, 633–660, doi:10.1175/1520-0434(2001)016<0633:SCIFHO>2.0.CO;2.

Lonfat, M., F. D. Marks, and S. S. Chen, 2004: Precipitation distribution in tropical cyclones using the Tropical Rainfall Measuring Mission (TRMM) microwave imager: A global perspective. *Mon. Wea. Rev.*, **132**, 1645–1660, doi:10.1175/1520-0493(2004)132<1645:PDITCU>2.0.CO;2.

Marchok, T., R. Rogers, and R. Tuleya, 2007: Validation schemes for tropical cyclone quantitative precipitation forecasts: Evaluation of operational models for U.S. landfalling cases. *Wea. Forecasting*, **22**, 726–746, doi:10.1175/WAF1024.1.

Meng, Z., and F. Zhang, 2008a: Test of an ensemble Kalman filter for mesoscale and regional-scale data assimilation. Part III: Comparison with 3DVAR in a real-data case study. *Mon. Wea. Rev.*, **136**, 522–540, doi:10.1175/2007MWR2106.1.

——, and ——, 2008b: Test of an ensemble Kalman filter for mesoscale and regional-scale data assimilation. Part IV: Comparison with 3DVAR in a month-long experiment. *Mon. Wea. Rev.*, **136**, 3671–3682, doi:10.1175/2008MWR2270.1.

Mlawer, E. J., S. J. Taubman, P. D. Brown, M. J. Iacono, and S. A. Clough, 1997: Radiative transfer for inhomogeneous atmospheres: RRTM, a validated correlated-k model for the longwave. *J. Geophys. Res.*, **102**, 16 663–16 682, doi:10.1029/97JD00237.

Ninomiya, K., 1984: Characteristics of Baiu front as a predominant subtropical front in the summer Northern Hemisphere. *J. Meteor. Soc. Japan*, **62**, 880–893.

Peng, S., and Coauthors, 2014: On the mechanisms of the recurvature of super typhoon Megi. *Sci. Rep.*, **4**, 4451, doi:10.1038/srep04451.

Qian, C., F. Zhang, B. W. Green, J. Zhang, and X. Zhou, 2013: Probabilistic evaluation of the dynamics and prediction of Supertyphoon Megi (2010). *Wea. Forecasting*, **28**, 1562–1577, doi:10.1175/WAF-D-12-00121.1.

Schaefer, J. T., 1990: The critical success index as an indicator of warning skill. *Wea. Forecasting*, **5**, 570–575, doi:10.1175/1520-0434(1990)005<0570:TCSIAA>2.0.CO;2.

Schumacher, R. S., and T. J. Galarneau Jr., 2012: Moisture transport into midlatitudes ahead of recurving tropical cyclones and its relevance in two predecessor rain events. *Mon. Wea. Rev.*, **140**, 1810–1827, doi:10.1175/MWR-D-11-00307.1.

Shi, W., J. Fei, X. Huang, X. Cheng, J. Ding, and Y. He, 2014: A numerical study on the combined effect of midlatitude and low-latitude systems on the abrupt track deflection of Typhoon Megi (2010). *Mon. Wea. Rev.*, **142**, 2483–2501, doi:10.1175/MWR-D-13-00283.1.

Skamarock, W. C., and Coauthors, 2008: A description of the Advanced Research WRF version 3. NCAR Tech. Note NCAR/TN-475+STR, 113 pp., doi:10.5065/D68S4MVH.

Stoelinga, M. T., 2009: A users' guide to RIP version 4.5: A program for visualizing mesoscale model output. University of Washington, accessed 30 July 2015. [Available online at http://www2.mmm.ucar.edu/wrf/users/docs/ripug.htm.]

Wang, C.-C., H.-C. Kuo, Y.-H. Chen, H.-L. Huang, C.-H. Chung, and K. Tsuboki, 2012: Effects of asymmetric latent heating on typhoon movement crossing Taiwan: The case of Morakot (2009) with extreme rainfall. *J. Atmos. Sci.*, **69**, 3172–3196, doi:10.1175/JAS-D-11-0346.1.

Wang, Y., Y. Wang, and H. Fudeyasu, 2009: The role of Typhoon Songda (2004) in producing distantly located heavy rainfall in Japan. *Mon. Wea. Rev.*, **137**, 3699–3716, doi:10.1175/2009MWR2933.1.

Wu, C.-C., and Y.-H. Kuo, 1999: Typhoons affecting Taiwan: Current understanding and future challenges. *Bull. Amer. Meteor. Soc.*, **80**, 67–80, doi:10.1175/1520-0477(1999)080<0067:TATCUA>2.0.CO;2.

——, T.-H. Yen, Y.-H. Kuo, and W. Wang, 2002: Rainfall simulation associated with Typhoon Herb (1996) near Taiwan. Part I: The topographic effect. *Wea. Forecasting*, **17**, 1001–1015, doi:10.1175/1520-0434(2003)017<1001:RSAWTH>2.0.CO;2.

——, and Coauthors, 2005: Dropwindsonde Observations for Typhoon Surveillance near the Taiwan Region (DOTSTAR): An overview. *Bull. Amer. Meteor. Soc.*, **86**, 787–790, doi:10.1175/BAMS-86-6-787.

——, K. K. W. Cheung, and Y.-Y. Lo, 2009: Numerical study of the rainfall event due to the interaction of Typhoon Babs (1998) and the northeasterly monsoon. *Mon. Wea. Rev.*, **137**, 2049–2064, doi:10.1175/2009MWR2757.1.

——, G.-Y. Lien, J.-H. Chen, and F. Zhang, 2010: Assimilation of tropical cyclone track and structure based on the ensemble Kalman filter (EnKF). *J. Atmos. Sci.*, **67**, 3806–3822, doi:10.1175/2010JAS3444.1.

——, S.-G. Chen, S.-C. Lin, T.-H. Yen, and T.-C. Chen, 2013: Uncertainty and predictability of tropical cyclone rainfall based on ensemble simulations of Typhoon Sinlaku (2008). *Mon. Wea. Rev.*, **141**, 3517–3538, doi:10.1175/MWR-D-12-00282.1.

Wu, L., Z. Ni, J. Duan, and H. Zong, 2013: Sudden tropical cyclone track changes over the western North Pacific: A composite study. *Mon. Wea. Rev.*, **141**, 2597–2610, doi:10.1175/MWR-D-12-00224.1.

Yamada, H., B. Geng, H. Uyeda, and K. Tsuboki, 2007: Thermodynamic impact of the heated landmass on the nocturnal evolution of a cloud cluster over a Meiyu–Baiu front. *J. Meteor. Soc. Japan*, **85**, 663–685, doi:10.2151/jmsj.85.663.

Yang, M.-J., D.-L. Zhang, and H.-L. Huang, 2008: A modeling study of Typhoon Nari (2001) at landfall. Part I: Topographic effects. *J. Atmos. Sci.*, **65**, 3095–3115, doi:10.1175/2008JAS2453.1.

——, S. A. Braun, and D.-S. Chen, 2011: Water budget of Typhoon Nari (2001). *Mon. Wea. Rev.*, **139**, 3809–3828, doi:10.1175/MWR-D-10-05090.1.

Yen, T.-H., C.-C. Wu, and G.-Y. Lien, 2011: Rainfall simulations of Typhoon Morakot with controlled translation speed based on EnKF data assimilation. *Terr. Atmos. Oceanic Sci.*, **22**, 647–660, doi:10.3319/TAO.2011.07.05.01(TM).

Yu, C.-K., and L.-W. Cheng, 2008: Radar observations of intense orographic precipitation associated with Typhoon Xangsane (2000). *Mon. Wea. Rev.*, **136**, 497–521, doi:10.1175/2007MWR2129.1.

——, and ——, 2013: Distribution and mechanisms of orographic precipitation associated with Typhoon Morakot (2009). *J. Atmos. Sci.*, **70**, 2894–2915, doi:10.1175/JAS-D-12-0340.1.

——, and ——, 2014: Dual-Doppler-derived profiles of the southwesterly flow associated with southwest and ordinary typhoons off the southwestern coast of Taiwan. *J. Atmos. Sci.*, **71**, 3202–3222, doi:10.1175/JAS-D-13-0379.1.

Zhang, F., Z. Meng, and A. Aksoy, 2006: Test of an ensemble Kalman filter for mesoscale and regional-scale data assimilation. Part I: Perfect model experiments. *Mon. Wea. Rev.*, **134**, 722–736, doi:10.1175/MWR3101.1.

——, Y. Weng, Y.-H. Kuo, J. S. Whitaker, and B. Xie, 2010: Predicting Typhoon Morakot's catastrophic rainfall with a convection-permitting mesoscale ensemble system. *Wea. Forecasting*, **25**, 1816–1825, doi:10.1175/2010WAF2222414.1.

Zhou, Y. S., S. T. Gao, and S. S. P. Shen, 2004: A diagnostic study of formation and structures of Meiyu front system over East Asia. *J. Meteor. Soc. Japan*, **82**, 1565–1576, doi:10.2151/jmsj.82.1565.